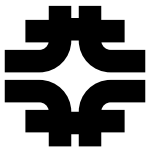

Fermi National Accelerator Laboratory

FERMILAB-Pub-97/142-E
E706

Calibration and Performance of the E706 Lead and Liquid-Argon Electromagnetic Calorimeter

L. Apanasevich et al.
The E706 Collaboration

Fermi National Accelerator Laboratory
P.O. Box 500, Batavia, Illinois 60510

March 1997

Submitted to *Nuclear Instruments and Methods A*

Disclaimer

Distribution

Calibration and performance of the E706 lead and liquid-argon electromagnetic calorimeter

Fermilab E706 Collaboration

L. Apanasevich [d], J. Bacigalupi [a], W. Baker [c], G. Ballocchi [j], M. Begel [j], R. Benson [e], S. Blusk [i], C. Bromberg [d], D. Brown [d], P. Chang [f], B. Choudhary [b], W. H. Chung [i], L. de Barbaro [j], W. DeSoi [j], W. Długosz [f], J. Dunlea [j], E. Engels, Jr. [i], G. Fanourakis [j], T. Ferbel [j], J. Ftacnik [j], D. Garelick [f], G. Ginther [j], M. Glaubman [f], P. Gutierrez [g], K. Hartman [h], J. Huston [d], C. Johnstone [c], V. Kapoor [b], J. Kuehler [g], A. Lanaro [j], C. Lirakis [f], F. Lobkowicz [j], P. Lukens [e], S. Mani [a], J. Mansour [j], A. Maul [d], R. Miller [d], B. Y. Oh [h], G. Osborne [j], D. Pellett [a], E. Prebys [j], R. Roser [j], A. Sinanidis [f], P. Shepard [i], R. Shivpuri [b], D. Skow [c], P. Slattery [j], L. Sorrell [d], D. Striley [f], W. Toothacker [h], N. Varelas [j], D. Weerasundara [i], J. J. Whitmore [h], G. Wu [f], T. Yasuda [f], C. Yosef [d], M. Zieliński [j] and V. Zutshi [b]

[a] *University of California-Davis, Davis, California 95616*

[b] *University of Delhi, Delhi, India 110007*

[c] *Fermi National Accelerator Laboratory, Batavia, Illinois 60510*

[d] *Michigan State University, East Lansing, Michigan 48824*

[e] *University of Minnesota, Minneapolis, Minnesota, 55455*

[f] *Northeastern University, Boston, Massachusetts 02115*

[g] *University of Oklahoma, Norman, Oklahoma 73019*

[h] *Pennsylvania State University, University Park, Pennsylvania 16802*

[i] *University of Pittsburgh, Pittsburgh, Pennsylvania 15260*

[j] *University of Rochester, Rochester, New York 14627*

Preprint submitted to Elsevier Science *20 May 1997*

Abstract

We report on the calibration and performance of a large lead liquid-argon electromagnetic calorimeter used by experiment E706 at Fermilab. The reconstructed π^0 mass was used to calibrate the energy response of the calorimeter. The systematic uncertainty in the linearity and uniformity of the mean energy response of the calorimeter after calibration was found to be less than $\pm 0.5\%$ for the sample of data analyzed. Detector characteristics, including sampling fluctuations and position resolution, are discussed.

Keywords: Sampling electromagnetic calorimeter; Calibration; Direct photons
PACS: 29.40.Vj; 29.30.-h

1 Introduction

Fermilab fixed-target experiment E706 was designed to measure high transverse momentum direct-photon production in hadronic interactions. These measurements provide tests of perturbative QCD and serve as a valuable tool for probing hadronic structure. The experiment also investigates jets produced in association with high-$P_{\rm T}$ photons or π^0's, and measures the inclusive production of high transverse momentum π^0, η, and ω mesons. Measurement of the direct-photon signal presents considerable experimental challenges because direct photons are produced at a rate of order 1 per 1000 hadronic jets, and those hadronic jets frequently contain π^0 or η mesons which decay electromagnetically, thus generating non-negligible background to the direct-photon signal. To perform this measurement, we designed and built a spectrometer optimized for the study of direct-photon production. The spectrometer included a charged-particle tracking system consisting of silicon microstrip detectors in the target region and multiwire proportional chambers and straw tube drift chambers downstream of a large aperture analysis magnet. This high-resolution tracking system provided precise measurements of charged-particle momenta and the locations of interactions of the incident beam particles in the targets. Photons were detected in a large lead and liquid-argon sampling electromagnetic calorimeter (EMLAC), located 9 m downstream of the target. The EMLAC acceptance was more than 1.5 units of pseudorapidity. Its readout was very finely segmented in radial and azimuthal views, allowing for separation of the two photons from π^0 decay for π^0 energies of up to 300 GeV. The radial segmentation was also used in the formation of a fast, localized high-$P_{\rm T}$ event selection trigger.

Since the yields of both direct photons and neutral mesons decrease dramatically with increasing transverse momentum, the uncertainties associated with these cross section measurements depend critically on the precise calibra-

tion of the energy response of the calorimeter. For example, for π^0's with $P_{\rm T} > \approx 10$ GeV/c, a 1% uncertainty in the energy scale calibration leads to more than 20% uncertainty in the π^0 cross section. Thus the establishment of an accurate and precise energy scale calibration is critical to the success of any such experiment. This report provides a summary of the data samples collected by E706, followed by a description of the EMLAC and the procedures used to calibrate its energy response. We illustrate the results of that calibration and present measurements of the intrinsic energy and position resolutions of the detector.

2 Data Samples

The Meson West Spectrometer, used to accumulate the E706 data samples, was commissioned during 1987. The initial data samples, accumulated during 1988, were obtained using 0.5 TeV/c π^- and p beams incident on Be and Cu targets, and had sensitivities of 0.5 events/pb and 0.8 events/pb, respectively. Publications based on these data contain brief descriptions of the spectrometer, trigger, and readout systems, and describe the results of the data analysis [1,2]. During 1990, a data sample with a sensitivity of $\approx$8 events/pb was obtained using a 0.5 TeV/c π^- beam incident on Be and Cu targets. During 1991, 0.5 TeV/c π^- and p beams incident on Be, Cu, and liquid H_2 targets were used to accumulate data samples with sensitivities of $\approx$2 events/pb and $\approx$9 events/pb, respectively. Data corresponding to $\approx$11 events/pb were also recorded for a 0.8 TeV/c p beam on Be, Cu, and H_2 targets during 1991. In addition to substantially greater statistical precision, the data collected in 1990 and 1991 have reduced systematic uncertainties by virtue of improvements made to the apparatus after the initial run. A faster data acquisition system [3] made it possible to read out the entire calorimeter, thus eliminating the *a priori* readout threshold ("zero suppression") imposed during the initial run. The faster data acquisition system also allowed for more frequent monitoring of the performance of the electronics. The increased redundancy and precision in the charged-particle tracking system [4], and the implementation of a liquid-hydrogen target (in 1991) were also significant improvements between the 1990 and 1991 runs and the initial run.

3 The Electromagnetic Calorimeter

The lead and liquid-argon sampling electromagnetic calorimeter [5,6] was assembled from four independent quadrants, each instrumenting $\frac{1}{4}$ of the azimuthal acceptance of the detector. Each quadrant was supported by stainless

steel plates along the quadrant and outer boundaries of the detector. These plates were bolted to 3.6 cm thick front and back G-10 plates which surrounded the sensitive part of the detector. The quadrants were assembled into an integrated detector, which has an inner radius of 0.2 m and an outer radius of 1.6 m. Figure 1 shows an exploded view of the EMLAC. After the quadrants were assembled, 3.2 mm thick copper plates with "fins" were bolted to the front and back G-10 plates to facilitate conduction of heat during the detector cooldown.

Each quadrant consisted of a stack of 66 layers. Each layer was composed of an absorber plate, a 2.5 mm liquid argon gap, a pair of octant-size 1.6 mm thick copper-clad G-10 anode boards, and another 2.5 mm liquid-argon gap. The absorber plate in the first layer was an aluminum sheet. In all other layers, the absorber plate was a 2 mm thick lead sheet. The thin absorber was selected to enhance the signal-to-noise ratio, while the argon gap thickness was chosen to provide an appropriate signal risetime (which allows for higher operating intensities) [6]. The EMLAC argon sampled $\approx$18% of the incident electron or photon energy, and was capable of sustained operation at interaction rates of 1 MHz.

The copper cladding of the G-10 anode boards in the odd-numbered layers was cut by a router to yield 254 radial strips centered on the nominal beam (Z) axis. The width of the strips on the first R anode board was 5.5 mm. The width of the R strips in the following odd-numbered layers increased slightly so that the radial geometry was projective relative to the target. The copper cladding of the interleaved even-numbered anode boards, referred to as Φ boards, was divided into two regions by a radial cut at 40 cm. In the inner region ($R < 40$ cm), the copper cladding on the Φ board was cut into azimuthal strips each of which subtends an azimuthal angle of $\pi/192$ radians, while each outer Φ strip subtends $\pi/384$ radians. The fine segmentation of the anode boards provides good position resolution and the capability to identify and separate two nearby showers. The R and Φ geometry facilitates implementation of the E706 event selection trigger based upon the detection of electromagnetic showers resulting from high transverse momentum particles.

During operation, the EMLAC was immersed in liquid argon and the absorber plates were connected to negative 2.5 kV high voltage supplies. Pairs of parallel 100 nF ballast capacitors were connected to each of the absorber plates to provide low impedance return paths for the signals generated by the motion of electrons liberated in the liquid argon by showering particles. Signals from corresponding strips on the R (and Φ) anode boards in the first 22 layers were connected together to generate the front section signals from the EMLAC. Signals from corresponding strips on the R (and Φ) anode boards in the remaining 44 layers were connected together to generate the back section signals. The front section consisted of 8.5 radiation lengths of material while the back

section was composed of 18 radiation lengths. This longitudinal segmentation helped in the separation of the two electromagnetic showers from the decay of a high-$P_{\rm T}$ π^0, and provided discrimination between showers generated by electromagnetically or hadronically interacting particles.

The EMLAC was suspended from four rods supported by a gantry capable of motion transverse to the beam. (The gantry provided the mechanism for directly exposing various locations in the calorimeter to incident beam particles for specialized calibration studies.) The gantry also supported an 8 interaction length hadronic calorimeter, which employed stainless steel as its absorber material. A 40-cm-diameter beam pipe, filled with helium gas, was inserted through the hole in the center of the calorimeters to minimize the density of material in that region. An insulated cylindrical stainless steel cryostat surrounded the calorimeter and was bolted to a warm mild steel flange on the gantry, and sealed via a very large O-ring. The region between the front of the EMLAC and the cryostat wall was occupied by an excluder vessel, a thin stainless steel shell filled with low density Rohacell foam. The total material between the downstream end of the target and the front of the instrumented region of the EMLAC corresponded to 2.8 radiation lengths.

The calorimeters were initially cooled to 95 K by cooling argon gas in the cryostat using an open circuit liquid nitrogen refrigeration system [7]. The cryostat was then filled with $\approx$70,000 liters of liquid-argon to submerge the calorimeters. The argon gas head above the liquid was maintained at a pressure of 2 psig by the liquid nitrogen refrigeration system.

The gantry also supported an electrically shielded Faraday room that housed the calorimeter readout electronics. Low impedance cables transferred the charge collected on the anode board strips via warm feedthrough boxes to electronics mounted in crates in the Faraday room. The signals were amplified, integrated, and digitized using electronics designed as part of the Fermilab RABBIT system [8,9]. The observed rise time of signals in the EMLAC was approximately 350 ns. "Fast-output" signals were generated by delay line differentiation of the signals from the charge sensitive amplifiers. These fast-output signals served as inputs to the high transverse momentum trigger system, while the signals themselves were delayed by 800 ns. Trigger modules weighted the fast-output signals from the R channels of the EMLAC by approximately the sine of the angle of the R channel relative to the nominal beam (Z) axis (assuming that the showering particle originated at the target) to provide a fast estimate of the transverse momentum detected in those channels. Other trigger modules summed these weighted signals from neighboring groups of strips and discriminated these summed signals to determine whether the event contained a candidate high transverse momentum shower of interest [10,4]. If an event satisfied a trigger, the integrated signals from each channel of the detector were sampled twice, once before the arrival of

the delayed signal and once near the peak of the delayed pulse. The difference between these two samples was digitized and read out. Measuring this difference minimized sensitivity to low frequency noise and energy depositions from earlier interactions.

The signals sent to and from the Faraday room passed through optical couplers or pulse transformers. The upgraded E706 data acquisition system was controlled by custom-made Fastbus-based Intelligent Control and Buffered Memory modules (ICBMs) [3]. These modules employed Motorola DSP 56001 signal processors and could accommodate 192k of 24 bit onboard memory, which was accessible to both the DSP processor and Fastbus. A total of 17 modules were used to process the data from the EMLAC and the hadronic calorimeter.

4 Pedestals and Gains

During the data acquisition phase of the experiment, online calibration tasks and data readout path verification checks were performed between Tevatron beam spills (approximately once every minute) [11]. The results of these operations were automatically monitored for deviations from previously recorded values. The calibration data, which included measurements of baseline pedestals and amplifier gains, were recorded about three times a day. Both pedestal and gain measurements were subsequently refined offline.

The online pedestal calibration constants were measured for each LAC channel by averaging the results of at least 128 consecutive readouts to determine each channel's mean baseline response in the absence of incident beam. The pedestals from this online calibration task served as the starting values for an offline pedestal evaluation that used non-interacting beam-triggered events and excluded those channels containing reconstructed showers [11]. These data-driven pedestal corrections, which were used in the final event reconstruction, were determined by calculating the average offsets detected for each individual channel over many beam events. The resulting pedestals were generally systematically shifted by a few ADC counts relative to the online pedestals. This shift may be attributed to pileup effects or differences in the average time between "triggers" during the calibration task and the beam-driven data acquisition. The uncertainties in the mean pedestal values resulting from the data calibration were within a few ADC counts (1 ADC count $\approx$ 3 MeV) over the entire data acquisition period. The RMS of the pedestal distribution for a typical channel was $\approx$60 MeV.

A small fraction of the events exhibited substantial noise/pileup effects, manifested by coherent shifts of the effective pedestal levels for a large number of channels in a given event. The frequency of these events increased during peri-

ods of significant accelerator spill structure that resulted in anomalously large instantaneous beam intensity [12]. An iterative procedure was employed to account for these coherent shifts on an event-by-event basis [13]. The procedure consisted of linear fits to the background level in the R and Φ channels, using only regions of the detector where no reconstructed showers were identified, to establish the "pedestal" level for each event. On average, this procedure resulted in modification of the pedestals by offsets that were $\leq$20 MeV per channel.

To achieve good energy resolution, it is necessary to account for the channel-to-channel variations in the electronic gains of the signal amplifiers and the differences in capacitance between the detector channels. Both of these characteristics were evaluated by measuring the individual channel responses to reference charges injected into the system [14]. The calibration hardware consisted of charge injection capacitors (2% precision) and a programmable voltage level generator (one for every 320 channels) operating according to the scheme designed by Fermilab's Particle Instrumentation Group for the RABBIT system. Charges of various magnitudes were injected into the amplifiers, and then collected and read out through the same electronic path used to record the data. The observed dependence of the collected charge on the voltage setting measures the relative gain variations between electronic channels. To improve the accuracy of the calibration procedure, the charge injection capacitors were calibrated relative to a common reference, and the effects of differences in voltage levels from different voltage generators were taken into account. The ADC gains measured using this method were stable over time to the $\pm$0.2% level. This stability is illustrated for the 1990 data in Fig. 2, where the gains of three typical channels are plotted as functions of time.

5 EMLAC Response

Since the response of liquid-argon calorimeters to incident particles is sensitive to electronegative impurities in the argon, the materials that were selected for use inside the cryostat were tested during the calorimeter design stage for release of electronegative impurities. A special order of fiberglass laminate G-10 without fire retardant was used in the detector to keep potential contaminants at a minimum. The components of the calorimeters were washed (with alcohol or oxyalic acid) or degreased to minimize introduction of dust and impurities. Once the calorimeters were completely installed, the cryostat containing the detector was tightly sealed, evacuated, and carefully checked for leaks, purged with gaseous-argon, and evacuated to < 0.1 Torr prior to cooldown.

The conditions for accepting the delivery of individual tankers of liquid argon required that the vendor certify that certain impurities were below specified

levels. In addition, the argon was required to satisfy two tests intended to detect electronegative impurities. Those tests were performed at our experimental hall prior to the acceptance of the liquid argon. The oxygen content of gas extracted from the tanker was evaluated using an electrochemical trace oxygen analyzer with sensitivity to ± 0.02 ppm oxygen [15]. For the second test, a sample of that gas was condensed in an ionization test cell that included a ^{106}Ru β source. The charge collected from the ionization gap was measured as a function of voltage applied across the gap and parametrized using the expression [16]:

$$Q = 2Q_{\circ}\frac{\lambda}{D}\left[1 - \frac{\lambda}{D}\left(1 - \mathrm{e}^{-D/\lambda}\right)\right] \tag{1}$$

where $Q_{\circ}$ is the plateau charge, D is the width of the ionization test cell argon gap, and λ is the mean free path length for the capture of conduction electrons by impurities in the liquid argon. The parameter λ was assumed to be proportional to the electric field $\mathcal{E}$ in the cell and inversely proportional to the concentration of impurities p (in parts-per-million), *i.e.*, $\lambda \equiv \alpha|\mathcal{E}|/p$, where α was taken to be 0.13 ± 0.03 ppm cm/(kV/cm) [17]. Only liquid-argon samples that measured less than 0.8 ppm oxygen equivalent contamination based on the results of fits of Eq. (1) to the ionization test cell data and the measurements from the trace oxygen analyzer were accepted for use in the initial run of the experiment. Prior to the 1990 run, the liquid argon was replaced, and only samples that measured less than 0.5 ppm oxygen equivalent contamination were accepted in this replacement process.

At the beginning of each fixed target run, a nominal 50 GeV/c electron beam incident on the calorimeter was used to verify the operation of the calorimeter and establish the trigger timing. Data accumulated using this electron beam were also used to evaluate the oxygen equivalent contamination of the liquid argon by measuring the response of the EMLAC to the electron beam as a function of the voltage across the argon gaps. Figure 3 shows the results of fits of Eq. (1) to the high voltage curve data accumulated early in the 1990 and 1991 runs. The shapes of both curves indicate a similar low level of oxygen equivalent impurities, $p < 1$ ppm.

The maximum collectable charge induced in the argon of an ideal LAr calorimeter (assuming argon ion motion, recombination, and electron capture by impurities are negligible) is given by the expression $Q_{\mathrm{th}} = efW/(2W_{\circ})$ [18], where e is the charge of the electron, W is the energy of the beam, $W_{\circ}$ is the ionization energy of one argon atom (23.6 ± 0.3 eV [19]), and f is the fraction of the incident electron's energy deposited in the liquid argon in the ionization gaps. Based on a detailed GEANT [20] simulation of electron shower development, $f = 0.18 \pm 0.02$ for the EMLAC. Thus, on average, a 50 GeV/c electron

incident on the EMLAC should liberate a collectable charge[1] of 29 ± 4 pC. Assuming that the translation from ADC counts to collected charge is constant, then the collected charge for an incident 50 GeV/c electron had an average of 12 ± 3 and 17 ± 4 pC (at the 2.5 kV operating voltage) at the beginning of 1990 and 1991 runs, respectively.[2]

The slow change in the response of the detector over time is illustrated in Fig. 4, which shows the increase in the mean reconstructed uncalibrated π^0 and η masses when plotted against "beam days" for the 1990 and 1991 runs. The beam days count excludes periods during which the beam was unavailable and the calorimeter high voltage was off, since no change was observed in the measured, uncalibrated meson masses before and after such periods. Figure 4 shows that the energy detected by the EMLAC for incident 50 GeV/c electron beams (measured during the high voltage curve data acquisition process) is consistent with the observed change in the uncalibrated π^0 and η masses.

Our measurements and studies indicate that the observed change in response is unlikely to be due to drifts in the high voltage or electronic noise. As reported in the preceding section, the measured electronic gains were also stable. The collected charge is sensitive to the integration times, and although several different choices of integration times were used during the data acquisition, those changes do not explain the observed monotonic time dependence of the response of the detector. This slow variation in the calorimeter response coupled with the apparent stability of the electronics leads to speculation that the change may be due to impurities in the ionizing medium and various possible mechanisms of electron capture. However, if impurities in the liquid argon were responsible, these impurities are not characterized by Eq. (1), and the impact of these impurities diminished over time.

The energy resolution of the EMLAC (as monitored via the width of the high-$P_{\rm T}$ π^0 and η signals as well as the differences in the measured energies of showers in the interleaved R and Φ views) was insensitive to this change in response of the detector as a function of time. Thus, even though we cannot provide an unambiguous explanation for the observed change in the response of the detector, we were easily able to compensate for this effect by a time-dependent scale factor. The observed time-dependence of the response of the detector was parametrized using the π^0 mass variation shown in Fig. 4. The energies of all particles reconstructed in the detector were corrected for this dependence as part of the reconstruction process (described below).

[1] The mean fraction of the electron energy lost in the inactive material in front of the EMLAC has been taken into account in this calculation.

[2] The conversion factor from ADC counts to charge deposited in the argon, even if presumed to be stable, is known only to $\leq 20\%$ accuracy.

6 Reconstruction of Electromagnetic Showers

The raw signals from the EMLAC were corrected to account for the measured pedestals. The gains were used to convert the detected signals from ADC counts to energy units. These energies were corrected for the time-dependent change in the response of the EMLAC, which was parametrized based upon a preliminary reconstruction of π^0 mesons in data sampled throughout the runs. The few dead channels in the detector (0.3% of the total channels) were assigned energy values interpolated from the contents of neighboring strips on an event-by-event basis.

After these preparatory steps, the energies from corresponding front and back section strips were added (forming a software "summed" section) prior to the shower search. The pattern recognition algorithm [21] searched through the summed R and Φ views independently for contiguous channels with energies above a minimum threshold of 80 MeV (95 MeV for the outer Φ region). As an illustration, Fig. 5 displays the energy deposited in a quadrant of the EMLAC for a typical event, with the energy in radial strips displayed separately for the "left" and "right" octants, and with the Φ channels divided into inner and outer regions. A "group" was defined as consisting of 3 or more consecutive strips each with energy above threshold, where at least one strip in the group had energy greater than 300 MeV, and the total energy in the group was more than 600 MeV.[3] Once the groups were identified, significant peaks within each group were found. A search through the front section energies corresponding to these groups was performed to determine whether there were additional peaks observable only in the front section of the EMLAC. For large energy depositions (above 35 GeV), the possible presence of two nearly overlapping showers was inferred from the behavior of the logarithmic derivative of the strip energy with respect to the distance from the peak position.

The energy and position of the showers detected in each view were determined by fitting the identified peaks with a two parameter shower shape function (see Fig. 6). This shower shape parametrization was determined from a sample of single photon showers generated by the GEANT-based E706 Monte Carlo, after establishing that the Monte Carlo results adequately described isolated showers observed in the data. The shower shape was found to be energy independent to a very good approximation [22]. For those groups containing multiple peaks, shower shape functions were simultaneously fit to each peak.

The showers detected in the R and Φ views were correlated based primarily upon their reconstructed energies. The spatial segmentation of the detector

[3] The parameters used to define a group were slightly different for the outer Φ region, where the individual strips subtended a larger area. The minimum number of strips in a group was two, and the peak strip threshold was 350 MeV.

into inner and outer Φ regions and left and right octants (radial strips), and the information about the longitudinal shower development in each view were also used in the correlation process. Energies of showers close to the boundaries of the detector were corrected for the fraction of the shower energy deposited outside the active area of the EMLAC. To account for accidental overlaps of showers in an individual view, the correlation algorithm allowed for the possibility of correlating two or more showers from one view with a single shower in the other view. More complicated correlation configurations were also accommodated (including special provisions for correlation of showers near the boundaries of the detector). Figure 5 illustrates the successful correlation of four showers in an event selected by a high-$P_{\rm T}$ trigger. The energy of the correlated showers was a sum of the energies, $E_R + E_\Phi$, of the R and Φ view showers. The momentum components associated with these showers were calculated from the shower energy and position as measured in the calorimeter, coupled with the assumption that the particles originated at the interaction vertex of the event (which was reconstructed using the information from the charged-particle tracking system).

7 Calibration of the EMLAC Energy Response

High statistics measurements of the reconstructed masses of π^0 mesons in the $\gamma\gamma$ decay mode were used to calibrate the energy response of the EMLAC [23,24]. The energy scale for photons was established by normalizing the reconstructed π^0 mass to its nominal (PDG [25]) value. The reconstructed η mass was used as a cross-check at each stage of the calibration. The $\pi^0\gamma$ decay mode of the ω meson was employed as an independent check of the results of the calibration. The comparison of the reconstructed ω mass to its accepted value provided a measure of the internal consistency between the two-photon and single photon energy scales.

A high quality electron sample was used to probe for evidence of residual effects. Numerous significant advances in understanding the calorimeter response were achieved using these electrons. The charged-particle tracking system determined the electron momenta (P) very precisely[4] and provided a sensitive, independently calibrated probe for the calorimetric energy measurement (E).[5] However, the electron shower shape in the calorimeter is slightly

[4] The tracking system momentum scale was calibrated [14] using the reconstructed $K^0_S \rightarrow \pi^+\pi^-$ and $J/\Psi \rightarrow \mu^+\mu^-$ signals, which were simultaneously within 0.1% of their PDG values. The resultant momentum scale was stable in time to within 0.25%.

[5] These E/P measurements served as the basis of the energy scale calibration for the 1988 data sample [1].

different than the photon shower shape due to differences in electron and photon shower development, and to the difference in the angle of incidence of electrons (which are affected by the momentum impulse of the magnet) and photons. In addition, since the π^0 (and η) signals provide high statistics probes of the higher energy part of the spectrum, those signals were used to calibrate (and check) the energy response of the EMLAC for the 1990 and 1991 data samples.

The results of any calibration procedure are, of course, sensitive to the method used and samples selected to perform that calibration. Calibrating to the nominal π^0 or η meson masses results in a small offset in the mean reconstructed energy of the individual single photons compared to their mean generated energies due to the slopes of the steeply falling production spectra as a function of the corresponding meson $P_{\rm T}$,[6] the resolution of the calorimeter, and the minimum $P_{\rm T}$ requirements invoked. The impact of this small offset ($\approx$1%) was subsequently taken into account in our physics analyses via the reconstruction efficiencies evaluated from our Monte Carlo samples.[7]

7.1 Data Sample Selection Criteria

A high quality electron sample was extracted using events in which a photon converted into an e^+e^- pair upstream of the magnet. Typically, such lepton pairs have reconstructed masses below 2 MeV/c^2, and they are referred to here as "Zero Mass Pairs" (ZMPs). These ZMPs were clearly identified through invoking geometric cuts on the information from the tracking system. The e^+e^- pair was generally reconstructed as a single track in the silicon microstrip detectors located upstream of the momentum analyzing dipole magnet. In the magnet, the pair separates due to the momentum impulse in the XZ plane induced by the magnetic field. The e^+ and e^- tracks were detected in the wire chambers located downstream of the magnet. A ZMP was defined as a pair of oppositely charged tracks with similar slopes in the YZ plane (the magnet non-bending plane) that intersected near the center of the magnet in the XZ plane. We used the sample of ZMPs in which both the e^+ and e^- tracks projected towards electromagnetic showers having at least 40% of their energy in the front section of the EMLAC to investigate the energy response of the detector.

Photons that contributed to the EMLAC energy scale calibration satisfied

[6] The slopes of the inclusive production spectra for π^0 and η mesons are very similar as functions of $P_{\rm T}$ [1].

[7] The Monte Carlo samples were weighted to insure that the spectra corresponded to the spectra measured in the data, and the response of the Monte Carlo simulation of the calorimeter was calibrated in the same manner as the data.

the following selection criteria: they were within the fiducial region of the detector; they deposited at least 20% of their energy within the front section of the calorimeter; and two- and three-photon combinations were restricted to showers in the same octant. Furthermore, the energy asymmetry of two-photon pairs, $A_{\gamma\gamma} \equiv |E_1 - E_2|/(E_1 + E_2)$, where E_1 and E_2 are the energies of the individual photons, was restricted to $A_{\gamma\gamma} < 0.5$.

The values of the reconstructed masses for high-$P_{\rm T}$ π^0's depend (at generally much less than the one percent level) on the spatial separation between the photons from the π^0. When the separation between showers is small, the sharing of the reconstructed energy between these two showers is determined less precisely than the sum of the two energies. Consequently, the resulting invariant mass is biased [24].[8] To minimize sensitivity to this mass reconstruction effect during the energy scale calibration, lower energy π^0's, that were selected via low-threshold triggers, were used. (Those π^0's had $P_{\rm T} > 2$ GeV/c for the 1990 data sample and $P_{\rm T} > 3$ GeV/c for the 1991 data sample.) Photons from η decays provided another data sample which minimized this separation-related bias.

7.2 The Calibration Procedure

Since the reconstructed two-photon mass depends upon both the reconstructed position of the showers in the EMLAC and the identified interaction vertex location in the target (assuming the photons originated at this vertex), the first step of the calibration procedure was to align the EMLAC relative to the charged-particle spectrometer. This was accomplished using a selected sample of ZMP electrons having momenta between 20 and 100 GeV/c. This sample provided a nearly azimuthally symmetric distribution of electrons across the face of the detector. Each EMLAC octant was independently aligned to the tracking system with the constraint that all octants had the same position along the Z axis.

For the next step in the calibration, the invariant masses of those photon pairs satisfying the requirements outlined in the preceding section were evaluated. The reconstructed energies of the showers contributing to these mass calculations were corrected to account for the average energy deposited in the inactive material in front of the EMLAC. A GEANT Monte Carlo simulation was used to evaluate this correction for the energy deposited in this inactive material. Figure 7 shows this average energy loss for photon- and electron-initiated showers as a function of the reconstructed shower energy. The mean mass of the π^0 signal observed in each octant of the detector relative to the

[8] Both data and Monte Carlo generated $\gamma\gamma$ pairs from π^0 decay exhibit a similar dependence of the reconstructed mass on separation.

nominal PDG value is shown in Fig. 8 for π^0's at a radius of $R > 50$ cm for the 1991 data samples. This pattern of relative scale variations was observed in each of the data samples.[9] This result was used to correct for the mean octant-to-octant variation in the energy response.

Figure 9 shows the values of π^0 and η masses as a function of R, the energy weighted radial position of the two photons from the neutral meson decay. A sample of ZMP electrons exhibits a similar radial dependence of the ratio of their calorimetric energy, E, to their momentum, P, measured in the tracking system (see Fig. 9). Since a similar radial dependence is exhibited in both two-photon samples and in the conversion electron sample, it is attributed to a remnant dependence of the EMLAC energy response on position in the detector. The details of the radial dependence may be sensitive to event structure and reconstructor biases, but the gross effect is directly correlated with the charge integration time, ΔT, used for the measurement of the EMLAC signals. Data recorded during the 1988, 1990, and 1991 runs employed different charge integration times; a comparison of the radial dependence of the reconstructed π^0 mass for these data sets is shown in Fig. 10. Had there been no significant difference in the pulse shape of signals generated by showers, and by the calibration procedure used in the measurement of the ADC gains, such radial dependences should have been accounted for by a gain calibration (with the appropriate integration times). However, since the pulse shapes were not identical, sensitivity to the specific choice of integration time was not entirely removed through the gain measurements, and hence the need for an additional correction. For each of the data samples presented in Fig. 10 (except the 1988 data), the observed radial dependence was parametrized independently for each octant. The energies of individual photons were corrected using these parametrizations.

7.3 Studies of the Calibrated EMLAC Response

Two-photon mass spectra generated after calibration are shown in Figs. 11 and 12 for the combined 1990 and 1991 data samples. These figures display the $\gamma\gamma$ invariant mass distributions in the π^0 and η mass regions, respectively, for photon pairs with $P_{\rm T} > 5$ GeV/c and energy asymmetry $A_{\gamma\gamma} < 0.5$. Requirements have also been invoked to exclude showers generated by incident beam halo muons. To insure that the two photons are well separated, entries in Fig. 11 satisfy the additional requirement that the energy weighted radial position of the pair of showers is further than 50 cm from the nominal beam axis. The calibrated, mean reconstructed π^0 and η masses in the $\gamma\gamma$ decay modes

[9] The variations may be due to several effects such as the differences in the construction and operation of each octant, and biases in the reconstruction algorithm.

are both within 0.1% of their nominal values. Figure 13 shows the invariant $\pi^0\gamma$ mass distribution in the vicinity of the ω mass, for $\pi^0\gamma$ combinations having $|\cos\theta^*| < 0.6$, where θ^* is the angle between the π^0 direction in the $\pi^0\gamma$ rest frame and the direction of the $\pi^0\gamma$ system in the lab frame. This mass plot includes both the 1990 and 1991 data samples, and showers generated by beam halo muons have been excluded. The reconstructed ω mesons provide an independent check on our energy scale calibration for reconstructed π^0's and single photons. Table 1 lists the means of gaussian fits to these signals, for the 1990 and 1991 data samples. The fitted masses are consistent with the nominal PDG values.

Figure 14 shows the dependence of the reconstructed mass of the η on the energy (top plot) and the $P_{\rm T}$ (bottom plot) of the $\gamma\gamma$ pair using the EMLAC energy scale calibration described in the previous section. Both plots illustrate the linearity of the energy calibration.

The calibrated EMLAC response was further investigated using the ZMP sample. Masses were evaluated for combinations of photons detected using the EMLAC and ZMPs measured using information from the tracking system. The mass spectrum for the three-particle γe^+e^- system is shown in Fig. 15 for two different minimum $P_{\rm T}$ requirements. This figure clearly exhibits π^0 and η mass peaks. Figure 16 shows the mean reconstructed mass of the η and away-side π^0 signals relative to their PDG values as a function of the energy of the γ within these γe^+e^- combinations. There is no significant systematic variation in either of the measured neutral meson masses as a function of the energy of the unconverted photon. This result indicates that the parametrization of the shower shape used to reconstruct photon energies was well-tuned to the data and demonstrates the linearity of the calibrated energy response of the EMLAC. The mean reconstructed γe^+e^- masses are $\approx 1\%$ below the PDG values for the π^0 and η mesons. This shift is attributed to energy loss by the e^+ and e^- due to bremsstrahlung in the target material. The mass of the reconstructed π^0 signal is shown in Fig. 17 as a function of the number of radiation lengths of target material traversed by the electrons for π^0's with $P_{\rm T} > 0.8$ GeV/c. The reconstructed π^0 mass clearly depends upon the number of radiation lengths traversed by the emerging electrons, and the reconstructed mass reaches the nominal value as the number of radiation lengths traversed by the conversion electrons vanishes. This is another indication that the absolute scale for single showers is set to the correct mean value. Figure 17 also shows that the mean π^0 mass reconstructed from pairs of photons that did not convert upstream of the analysis magnet is independent of the amount of material traversed in the target.

The extensive tests of the energy scale calibration, using independent sets of data, indicate that the resultant uncertainty in the energy scale calibration is less than 0.5%.

8 Other Features

As previously indicated, the segmentation of the readout of the EMLAC into independent front and back sections provides information used in the correlation of showers reconstructed in R and Φ views. Furthermore, this longitudinal segmentation provides discrimination against hadronically induced showers. Figure 18 displays the distribution of energy deposited in the front of the EMLAC relative to the total energy in the EMLAC for showers from incident electrons and hadrons. The electron distribution is strongly peaked at $E_{\rm front}/E_{\rm total} \approx 0.9$. The corresponding distribution for photons exhibits a similar character. Figure 18 also shows the $E_{\rm front}/E_{\rm total}$ distribution for incident charged particles that are primarily pions from the decays of K^0_S. Hadrons that deposit sufficient energy in the EMLAC to be reconstructed have an $E_{\rm front}/E_{\rm total}$ distribution peaked near 0.1. Showers with $E_{\rm front}/E_{\rm total}$ less than 0.2 are generally excluded from our analyses of electromagnetic shower candidates.

For those incident particles that deposit sufficient energy in both the front and back sections of the EMLAC, the incident direction of the particles can be determined. This information on incident direction can be valuable in discriminating against showers due to particles that do not originate in the target. Such showers are due primarily to those beam halo muons generated in the primary target dump that were not swept away from the spectrometer by the beamline "spoiler" magnets. The design of the beamline, target, and dump were intended to minimize the rate of beam halo muons incident on the spectrometer. Nevertheless, the high-$P_{\rm T}$ triggers were sensitive to showers generated by these halo muons, and the additional directional discrimination served as a valuable tool in identifying and eliminating those muon induced showers not rejected by the veto requirements built into the trigger system. The incident direction of showers observed in the EMLAC was characterized as $\delta \equiv R_{\rm front} - (Z_{\rm front}/Z_{\rm back})\, R_{\rm back}$, where $R_{\rm front}$ and $R_{\rm back}$ are the radial positions of the reconstructed shower in the front and back sections, and $Z_{\rm front}$ and $Z_{\rm back}$ are the longitudinal locations of those EMLAC sections relative to the nominal target location. Obviously, showers with δ near zero are generated by particles which come from the direction of the target, while showers with large δ were generated by particles incident from other directions. Figure 19 shows the δ distributions for showers identified as incident photons (solid histogram) and as incident beam halo muons (dashed histogram). Note that the beam halo muon induced showers are easily discriminated from the showers due to photons from the target region.

The electronics designed and implemented for the readout of the liquid argon calorimeter included timing circuitry to provide information on the arrival time of detected showers [8]. This timing information allowed for discrimi-

nation against showers associated with out-of-time interactions or beam halo muons. Signals from four neighboring LAC amplifier channels were added together, and this output differentiated and compared to a crate-wide threshold. If the signal was above threshold, then the timing circuit was activated. The circuit employed a common stop—the timer stopped upon receipt of a trigger signal. Once the timing circuit was activated, a second circuit could be enabled by another energy deposition in the same set of four LAC channels. That second timing circuit was also stopped by the same common stop signal. The timing circuits were reset if there was no trigger signal within about 1.5 μs. Figure 20 illustrates the performance of these time-to-voltage converters (TVCs) for rare events selected specifically because an additional interaction was detected 38 ns after the in-time interaction via the interaction scintillation counters. This figure shows clear evidence of π^0 production associated with both the in-time and the out-of-time interactions, and illustrates the resolution of the timing circuit.

9 Sampling Fluctuations

Sampling fluctuations in the EMLAC energy measurements were evaluated using energies measured in the interleaved R and Φ views (E_R and E_Φ). Since there was an absorber plate between each R anode board layer and each Φ anode board layer, the measurement of the difference between E_R and E_Φ was sensitive to several effects that contribute to the energy resolution of the detector, including the statistical fluctuations in the number of e^+e^- pairs sampled, the fluctuations of the energy deposits in liquid-argon (Landau fluctuations), and the path-length fluctuations due to multiple scattering in the transverse shower development [26].

We studied the widths of the $E_R - E_\Phi$ distributions as a function of the shower energy ($E = E_R + E_\Phi$) in a sample of well-isolated showers,[10] fully contained within the fiducial volume of the detector. Figure 21 shows the dependence of $\sigma(E_R - E_\Phi)/E$ on shower energy, measured separately in the inner and outer regions of the EMLAC. The distributions were fit using the form $\sigma^2/E^2 = A^2/E + B^2/E^2 + C^2$. The fits resulted in similar values for the sampling term A for both regions. These fits yielded effectively zero ($< \pm 90$ MeV) for the parameter B for the isolated single photon data samples. The fits to the 1990 (1991) data from the outer region of the detector yielded 0.1476 ± 0.0014 GeV$^{1/2}$ (0.1465 ± 0.0008 GeV$^{1/2}$) for the sampling term $A_{\rm O}$, and 0.0098 ± 0.0004 (0.0145 ± 0.0002) for the constant term $C_{\rm O}$. The

[10] Since the correlation algorithm matches showers by minimizing $E_R - E_\Phi$, it introduces a bias in the measurement of sampling fluctuations based upon this difference. However, this bias is minimized in a sample of well-isolated showers.

fits of the 1990 (1991) inner region data yielded $A_{\rm I} = 0.1397 \pm 0.0006$ GeV$^{1/2}$ (0.1375 ± 0.0019 GeV$^{1/2}$) and $C_{\rm I} = 0.0000 \pm 0.0017$ ($C_{\rm I} = 0.0085 \pm 0.0003$). Fits to $\sigma(E_R - E_\Phi)/E$ measured from two-photon data samples yielded sampling terms consistent with the values reported here, noise terms consistent with expectations based upon the observed RMS of the pedestals, and constant terms about 15% larger than those measured from the isolated single photon samples.

Since $\sigma(E_R - E_\Phi)$ is not sensitive to correlated fluctuations in E_R and E_Φ, it need not be a complete measure of the energy resolution of the detector. Nevertheless, this measurement is of particular importance to E706 since the photon reconstruction algorithm uses E_R and E_Φ to correlate the showers detected in the R and Φ views in order to reconstruct the locations of photons in the detector. Our detailed GEANT Monte Carlo simulations were adjusted to adequately represent the observed $\sigma(E_R - E_\Phi)$.

A simple Monte Carlo simulation was constructed using parameterizations of the energy loss in the material upstream of the detector and the characteristics of the EMLAC reported in this paper along with the assumption that the intrinsic energy resolution of the EMLAC was equivalent to the measured $\sigma(E_R - E_\Phi)$. Using the measured cross sections as input, this simulation reproduced the reconstructed widths of the observed neutral meson mass peaks. This result from this simple model indicates that any correlated fluctuations between the measured E_R and E_Φ do not significantly contribute to the mass resolution of the EMLAC.

10 Position Resolution

The position resolution of the EMLAC was measured using ZMP electrons via the widths of the ΔX and ΔY distributions. ΔX and ΔY are the differences in the X and Y views between the reconstructed positions of the electron shower in the calorimeter and the position of the corresponding track projected to the face of the EMLAC as measured by the charged-particle tracking system. The contributions to the widths due to the resolution of the tracking system varied from a few percent to 15%. These contributions were assumed to be uncorrelated with the the EMLAC position resolution and were subtracted out in quadrature. Figure 22 shows the position resolution of the EMLAC as a function of the shower energy, $\sigma_{\Delta r} \equiv \sqrt{\sigma^2_{\Delta X} + \sigma^2_{\Delta Y}}$. For large energy showers, the position resolution of the EMLAC was better than 600 μm. A fit of the data to the form $\sigma_{\Delta r}(E) = a/E + b$ yielded $a = 1.65 \pm 0.01$ GeV cm and $b = 0.045 \pm 0.001$ cm.

11 Summary

A finely-segmented lead and liquid-argon electromagnetic calorimeter was designed and built for a high-$P_{\rm T}$ direct-photon experiment performed at Fermilab. The energy response of the calorimeter was calibrated using π^0's. After calibration, the response of the detector was found to be uniform and linear over this data sample to better than 0.5%. The mass resolution for the high-$P_{\rm T}$ π^0 signals was 6 MeV/c^2. The mass resolution for high-$P_{\rm T}$ η mesons was < 20 MeV/c^2. The detector was capable of resolving two photons from π^0 decays for π^0's of energy up to 300 GeV. The position resolution of the detector for high energy photons was better than 600 μm.

Acknowledgement

We are grateful to our colleagues who contributed to bringing the Meson West spectrometer into existence, participated in the initial E706 run, and generated a substantial fraction of the software used in reconstructing the data sample from the second run. We thank the U. S. Department of Energy, the National Science Foundation, including its Office of International Programs, the Universities Grants Commission of India, and Fermilab for their support of this research.

References

[1] G. Alverson *et al.*, Phys. Rev. D **48**, 5 (1993).

[2] G. Alverson *et al.*, Phys. Rev. D **49**, 3106 (1994).

[3] C. Lirakis, in *Proceedings of the First Annual Conference on Electronics for Future Colliders, May 22-23, 1991* (Le Croy Corp., Chestnut Ridge, New York, 1991), p. 35.

[4] L. Apanasevich *et al.*, FERMILAB-Pub-97/030-E, hep-ex/9702014, (to be published in Phys. Rev. D) (1997).

[5] F. Lobkowicz *et al.*, Nucl. Instrum. Methods Phys. Res. A **235**, 332 (1985).

[6] W. DeSoi, Ph.D. thesis, University of Rochester, 1990.

[7] J. Urbin *et al.*, in *Advances in Cryogenic Engineering, Proceedings of the 1989 Cyrogenic Engineering Conference, July 24-28 1989, UCLA, California*, edited by R. W. Fast (Plenum Press, New York, 1990), Vol. 35, Part B, p. 1803.

[8] D. D. Skow, Ph.D. thesis, University of Rochester, 1990.

[9] G. Drake *et al.*, Nucl. Instrum. Methods Phys. Res. A **269**, 68 (1988).

[10] L. Sorrell, *The E706 Trigger System*, E706 Note 201, 1994 (unpublished); Ph.D. Thesis, Michigan State University, 1995.

[11] N. Varelas, Ph.D. thesis, University of Rochester, 1994.

[12] C. Moore, in *Fermilab Report, Fall 1992*, edited by C. Crego (Fermilab Publications Office, Batavia, Illinois, 1992), p. 12.

[13] G. Osborne, Ph.D. thesis, University of Rochester, 1996.

[14] L. de Barbaro, Ph.D. thesis, University of Rochester, 1995.

[15] Delta F Trace Oxygen Analyzer, Model FA30111SA, Delta F Corporation, 15 Constitution Way, Woburn, MA 01801.

[16] W. Hofmann *et al.*, Nucl. Instrum. Meth. **135**, 151 (1976).

[17] J. Engler *et al.*, Nucl. Instrum. Meth. **133**, 521 (1976).

[18] W. J. Willis and V. Radeka, Nucl. Instrum. Meth. **120**, 221 (1974).

[19] M. Miyajima *et al.*, Phys. Rev. A **9**, 1438 (1974); **10**, 1452 (1974).

[20] R. Brun *et al.*, GEANT3 User's Guide CERN DD/EE/84-1, (1987).

[21] W. Długosz, Ph.D. thesis, Northeastern University, 1994.

[22] R. Roser, Ph.D. thesis, University of Rochester, 1994.

[23] N. Varelas *et al.*, Nucl. Phys. B (Proc. Suppl.) **44**, 153 (1995).

[24] M. Begel, Ph.D. thesis, University of Rochester, in preparation.

[25] Particle Data Group, R. M. Barnett *et al.*, Phys. Rev. D **54**, 1 (1996).

[26] C. W. Fabjan, in *Techniques and Concepts of High-Energy Physics III*, edited by T. Ferbel (Plenum Press, New York, 1985), p. 281.

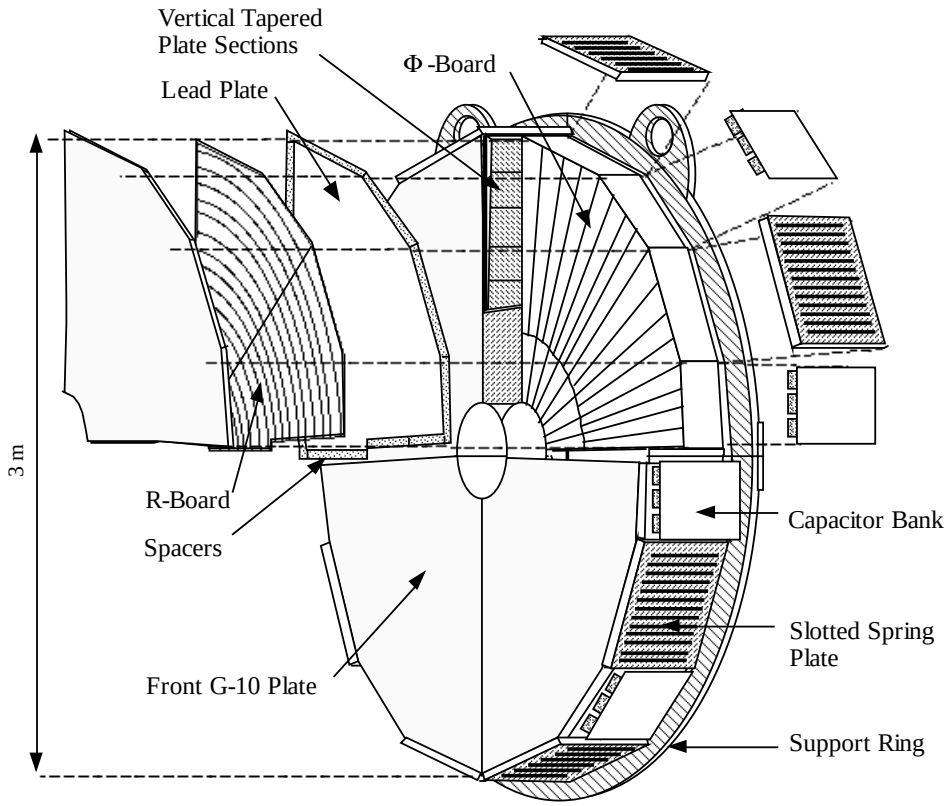

Fig. 1. Illustration of the EMLAC showing the anode boards with radial (R) and azimuthal (Φ) strips.

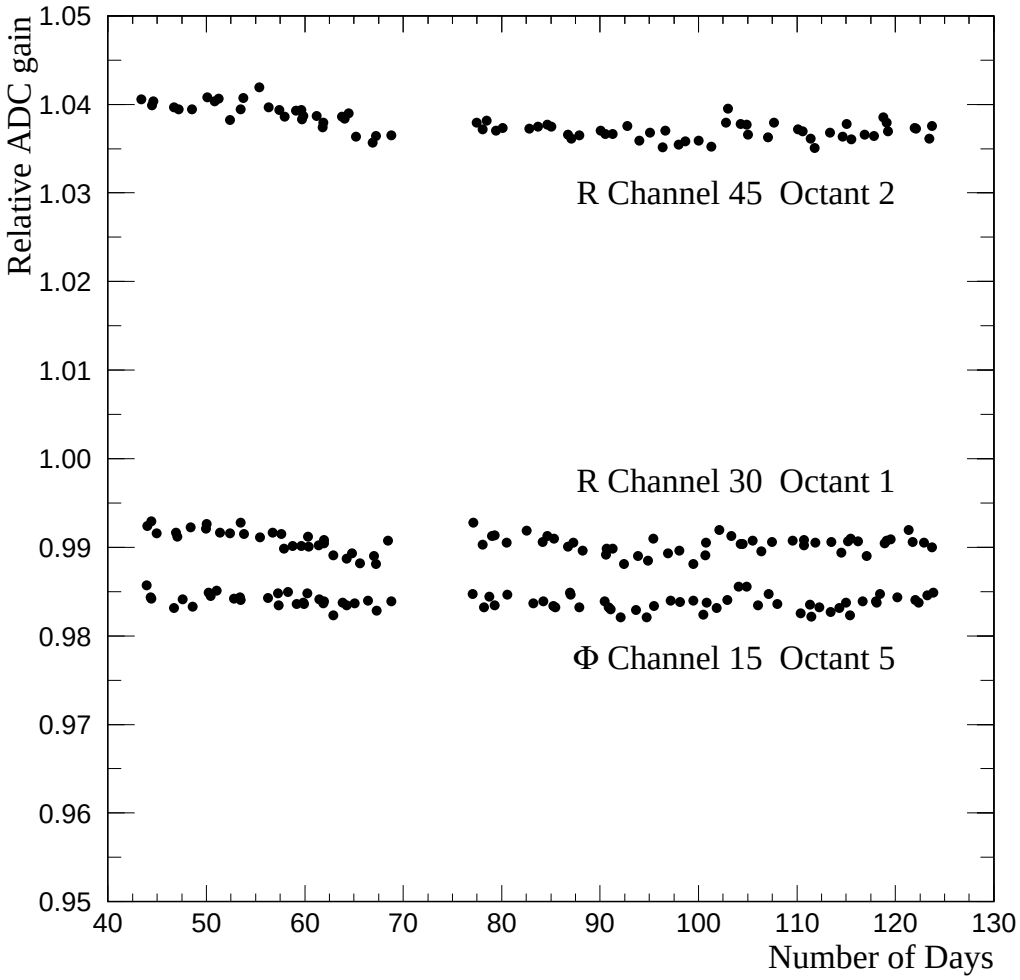

Fig. 2. ADC gain values for three typical channels, as functions of time, compared to the mean for all channels.

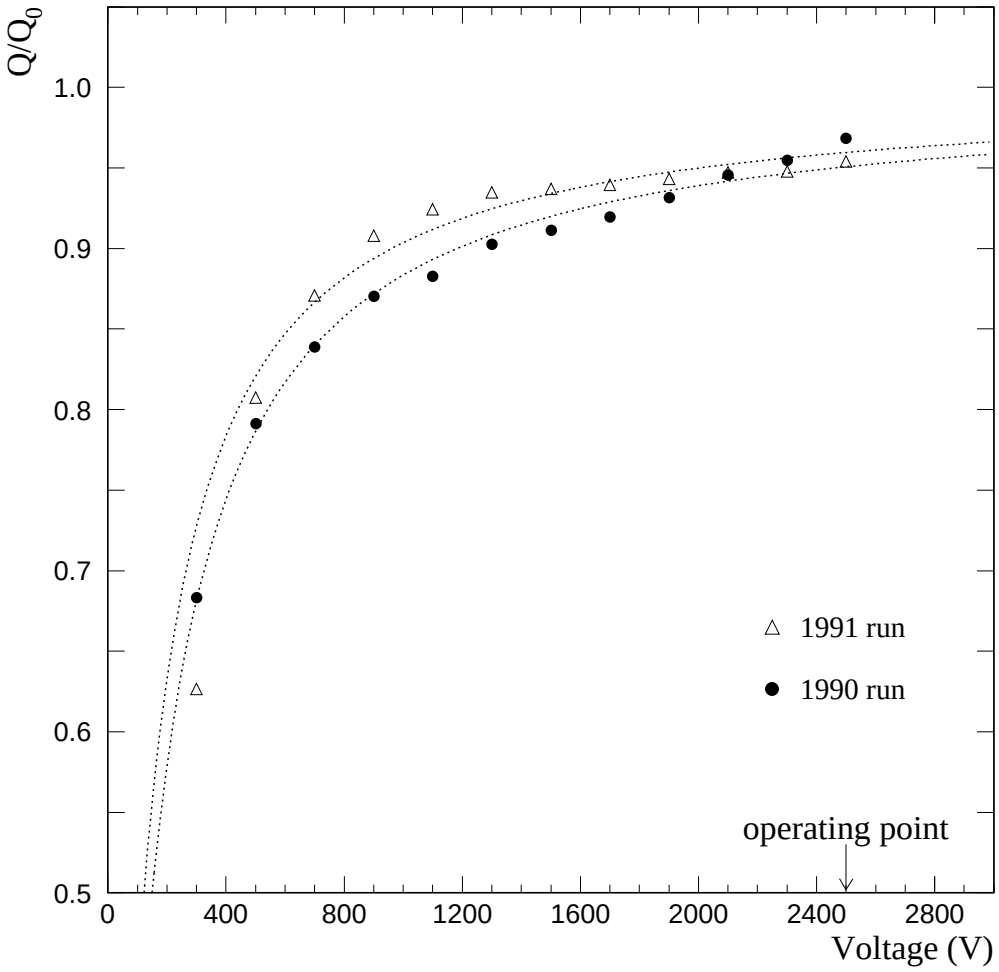

Fig. 3. Collected charge (normalized to the plateau charge Q_o) as a function of the voltage applied across the argon gaps of the EMLAC for incident 50 GeV/c electron beams at the beginning of the 1990 and 1991 runs. The curves are fits to Eq. (1) as described in the text.

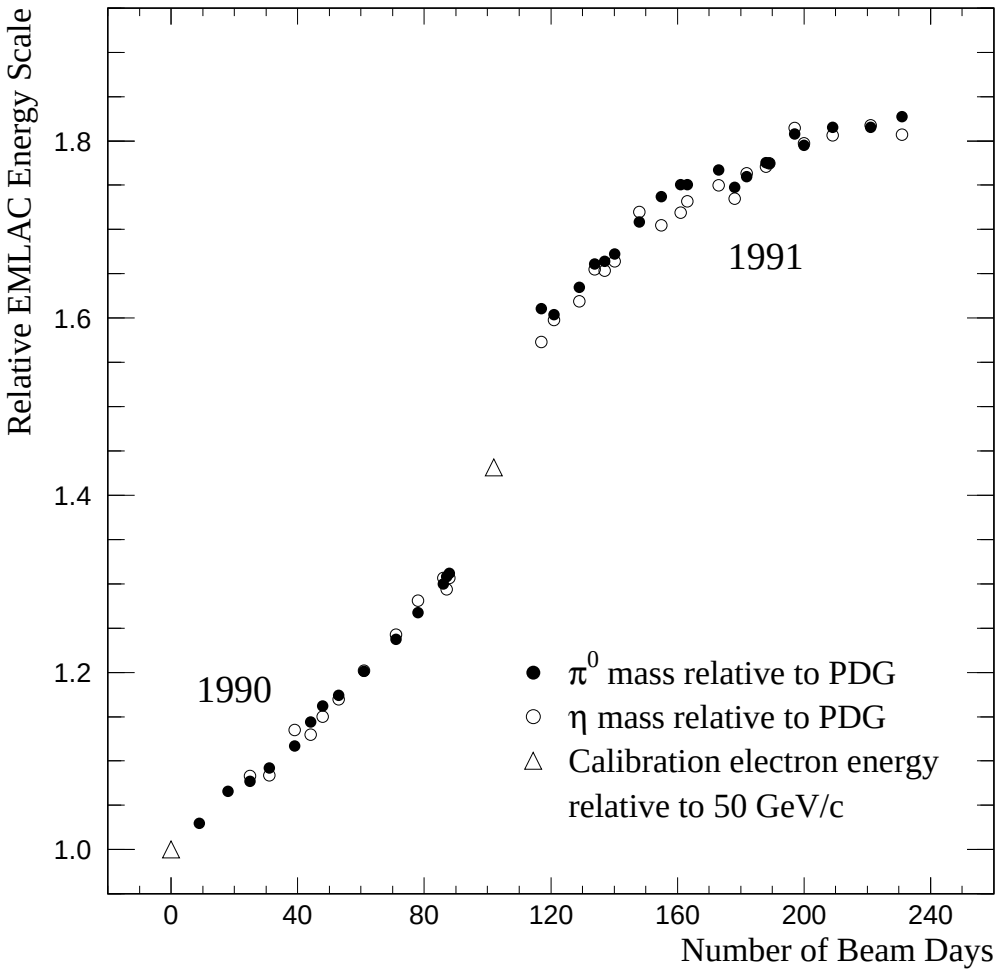

Fig. 4. Uncalibrated relative values for the reconstructed masses of the π^0 and η signals as a function of "beam days" (see text) during the 1990 and 1991 runs. The triangles represent the EMLAC response to 50 GeV/c incident electron beams. The π^0 and η mesons were reconstructed in the region of the detector between 50 and 150 cm in radius.

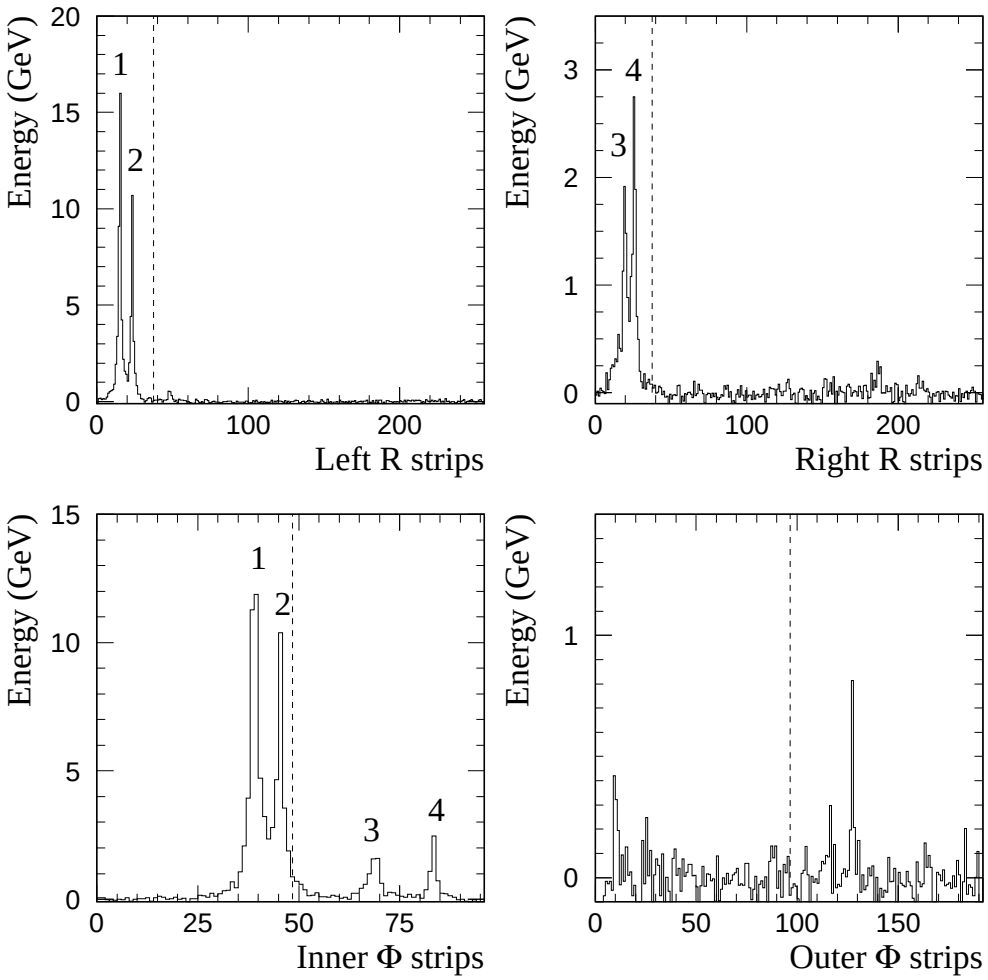

Fig. 5. A display of the energy observed in R and Φ strips of a quadrant of the EMLAC for a single event. Energies from corresponding strips in the front and back sections have been added together in this display of the "summed" section. The R strips are divided into "left" and "right" octants, while the Φ strips are divided into inner (R <40 cm) and outer (R >40 cm) regions. Dashed lines mark the location of the boundaries in the other (interleaved) view. Showers tagged with the same numbers were correlated by the reconstruction program.

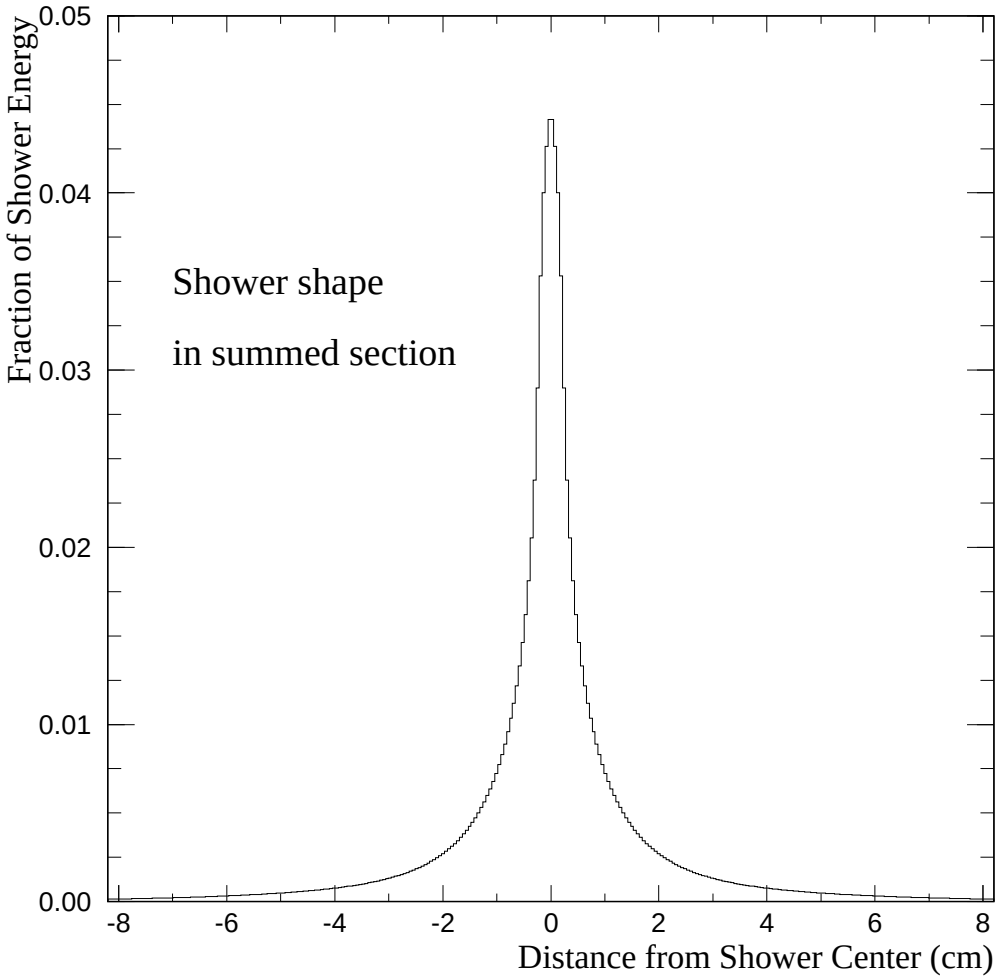

Fig. 6. Photon shower shape as a function of the distance from the center of the shower as determined via a Monte Carlo simulation.

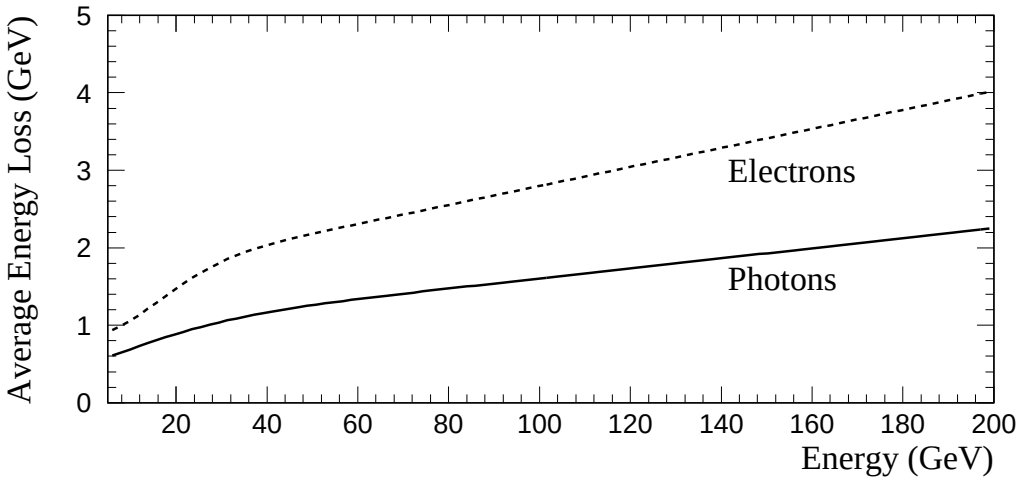

Fig. 7. Average energy loss for photons and electrons as a function of the reconstructed shower energy as determined from the Monte Carlo simulation.

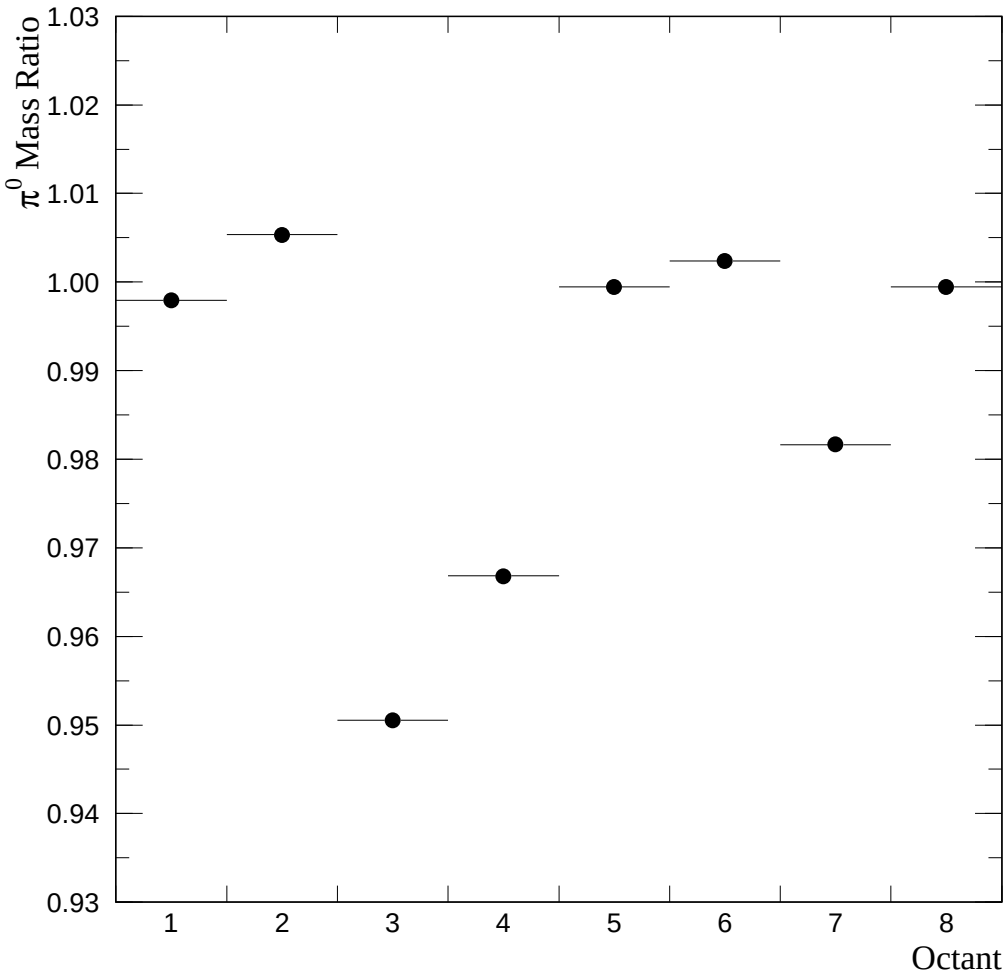

Fig. 8. The mean π^0 mass measured in each octant normalized to the PDG value. The π^0's have $P_{\mathrm{T}} > 3.0$ GeV/c and the energy weighted radial positions of the pairs of photons are greater than 50 cm.

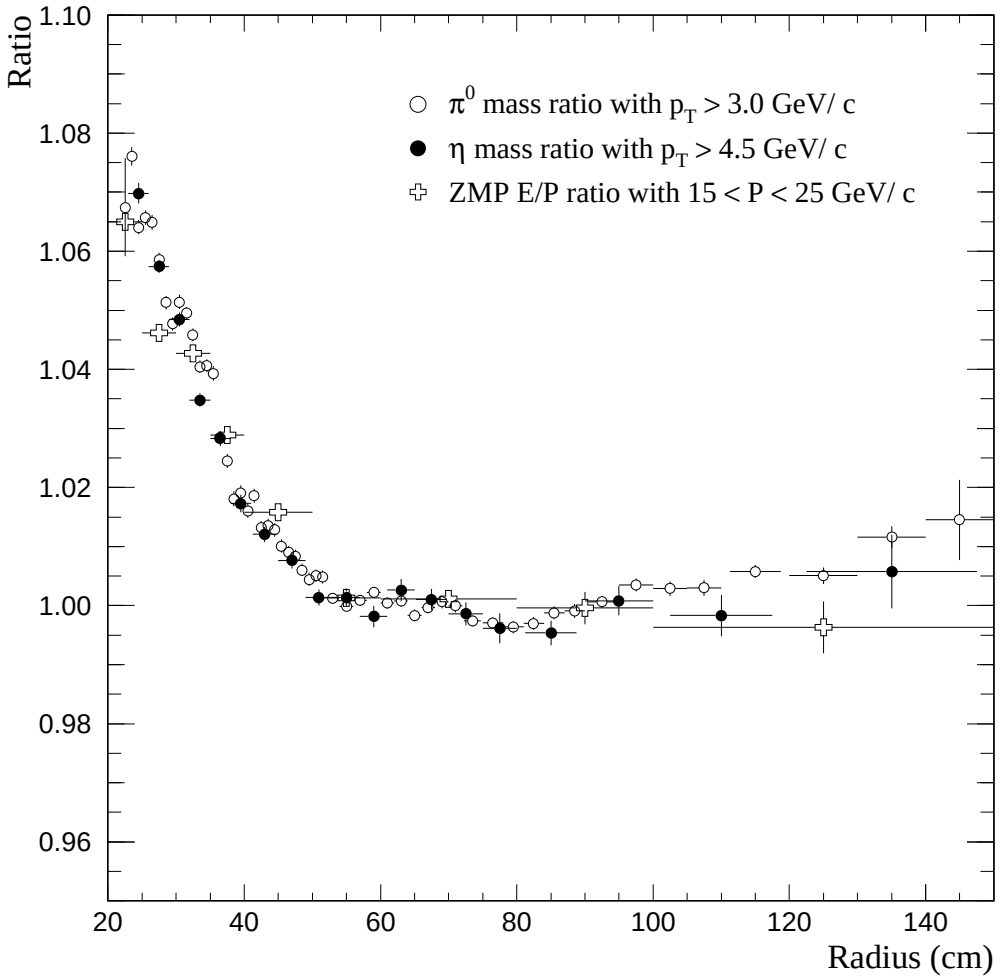

Fig. 9. The reconstructed $\pi^0$and η masses (normalized to the PDG values) as a function of the R position of the mesons in the EMLAC. The radial dependence of the E/P ratio for ZMP electrons is also shown. The data are from the 1991 run.

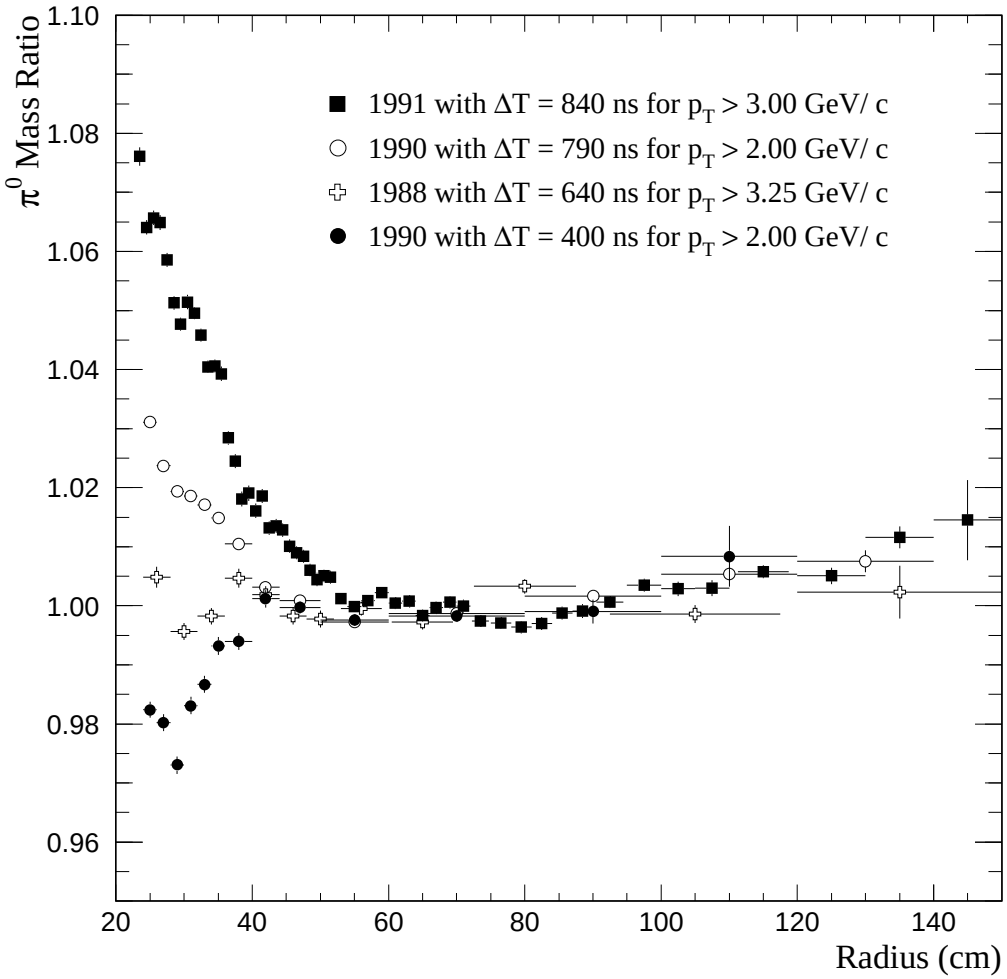

Fig. 10. Radial dependence of the reconstructed π^0 mass normalized to the PDG value for several choices of the EMLAC charge integration time.

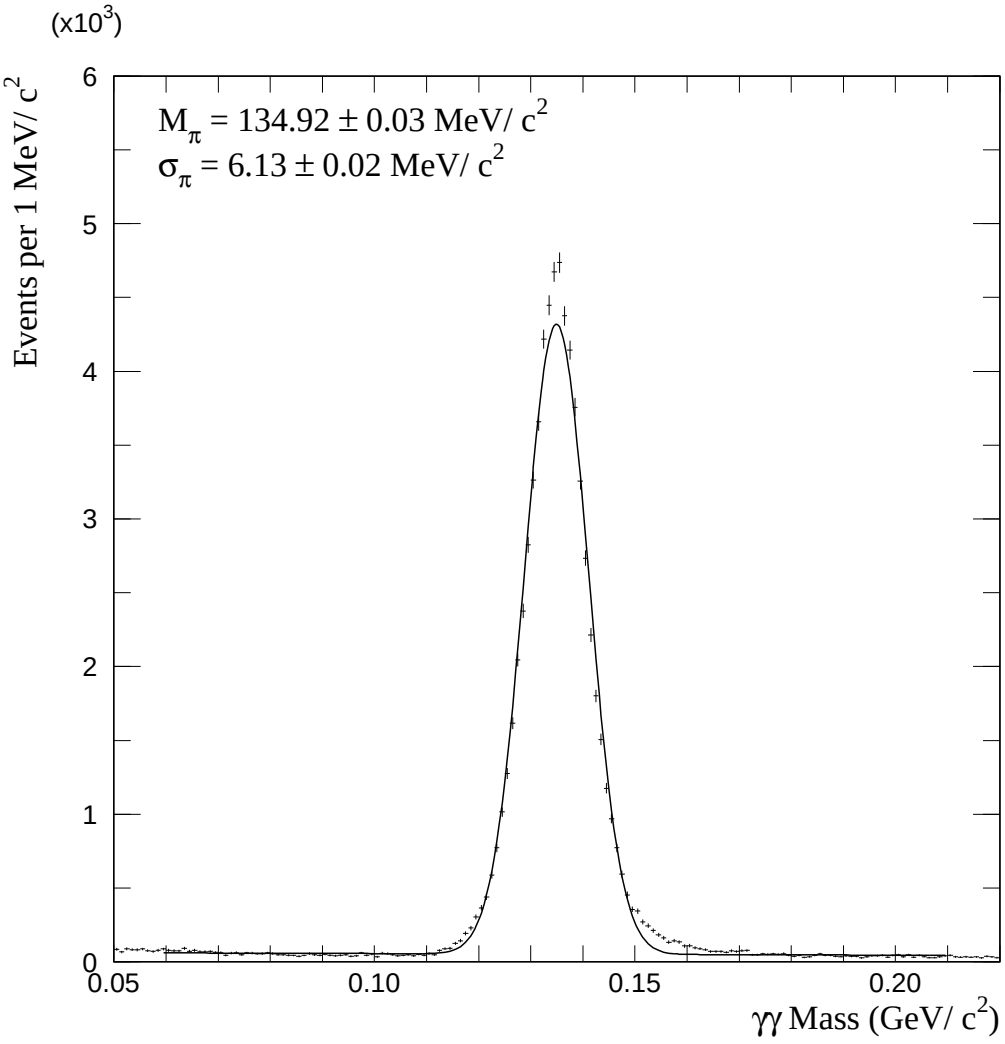

Fig. 11. The calibrated two-photon mass distribution in the π^0 mass region for $\gamma\gamma$ pairs with $P_{\rm T} > 5$ GeV/c and energy asymmetry $A_{\gamma\gamma} < 0.5$. These photon pairs are more than 50 cm from the beam axis (see text for details).

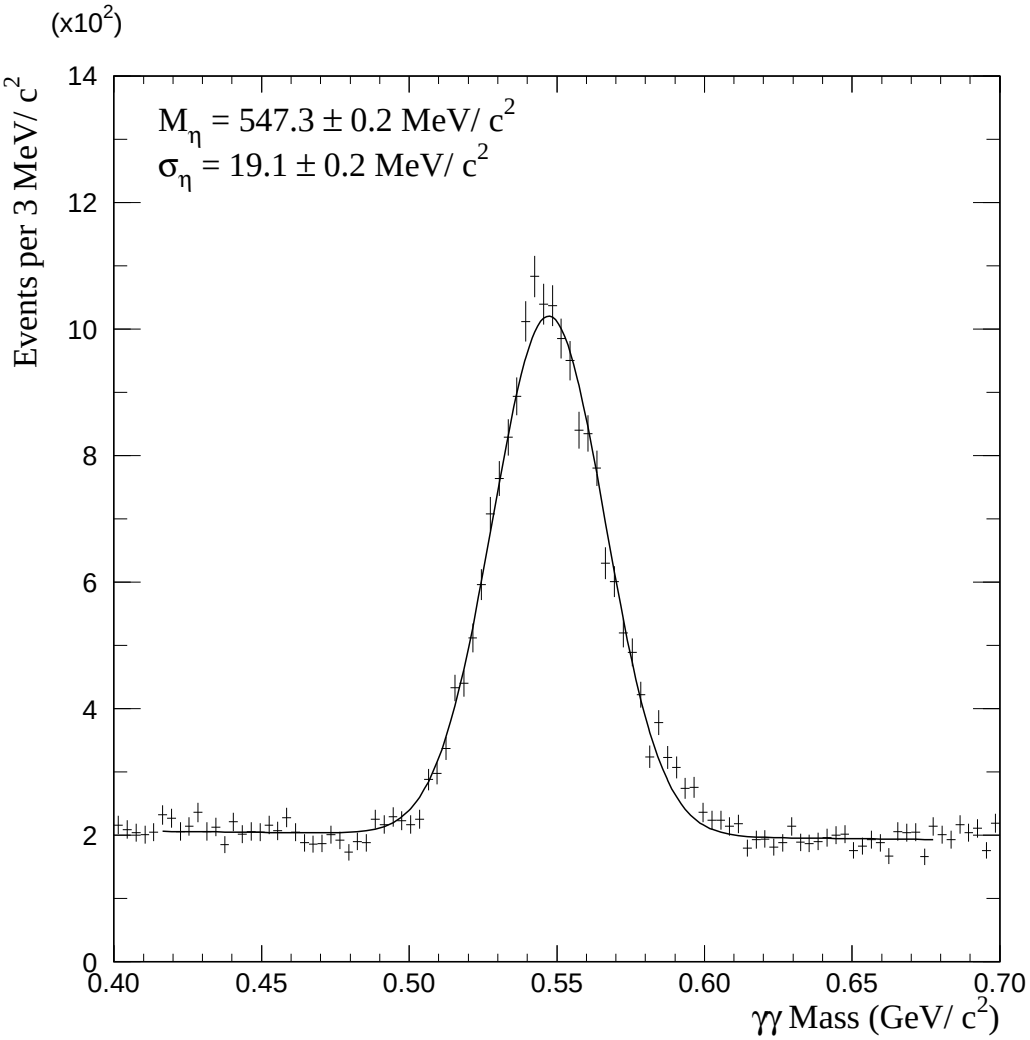

Fig. 12. The calibrated two-photon mass distribution in the η mass region for $\gamma\gamma$ pairs with $P_{\rm T} > 5$ GeV/c and energy asymmetry $A_{\gamma\gamma} < 0.5$.

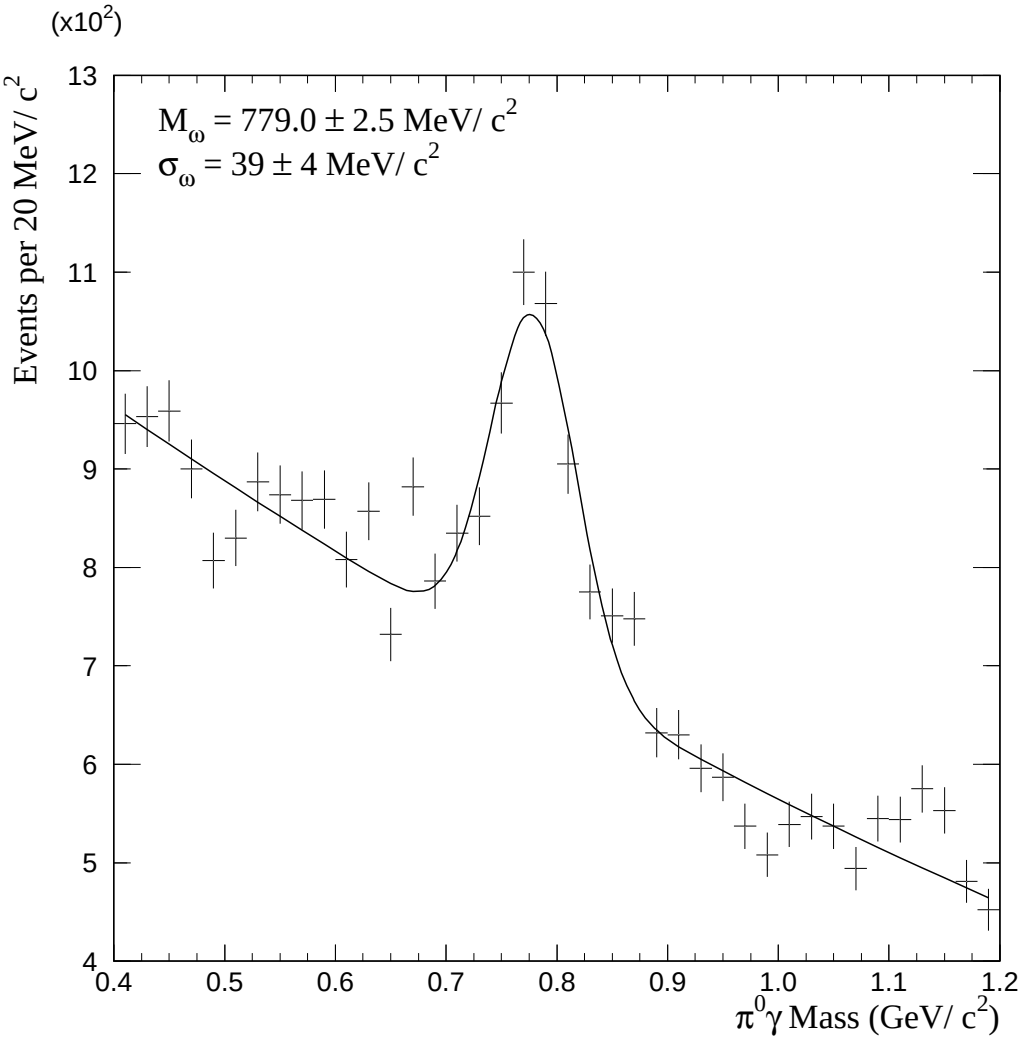

Fig. 13. The calibrated $\pi^0\gamma$ mass distribution in the ω mass region for $\pi^0\gamma$ combinations with $P_{\rm T} > 5$ GeV/c, π^0 energy asymmetry $A_{\gamma\gamma} < 0.5$, and $|\cos\theta^*| < 0.6$ for the $\pi^0\gamma$ combinations.

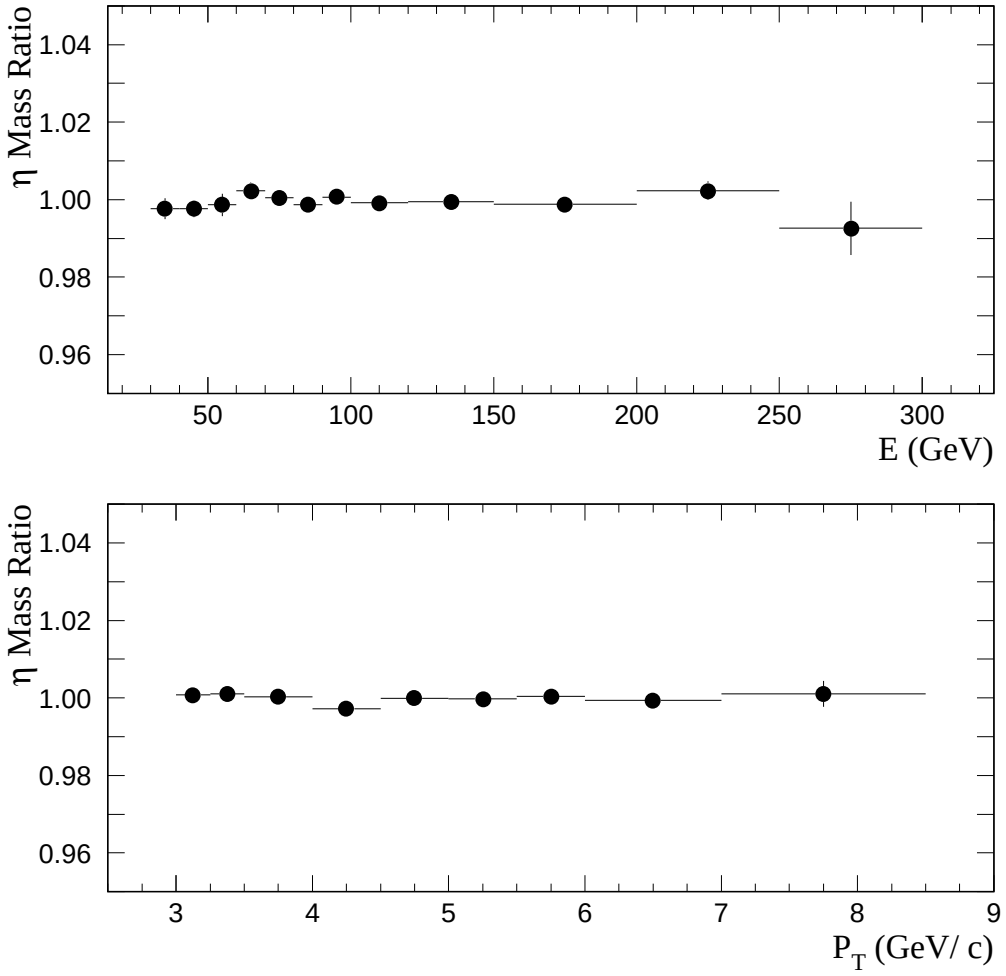

Fig. 14. Ratio of the mass of the η signal in the $\gamma\gamma$ decay mode to its nominal value as a function of energy (top plot) and P_{T} (bottom plot) of the $\gamma\gamma$ pair. The data are from the 1991 run.

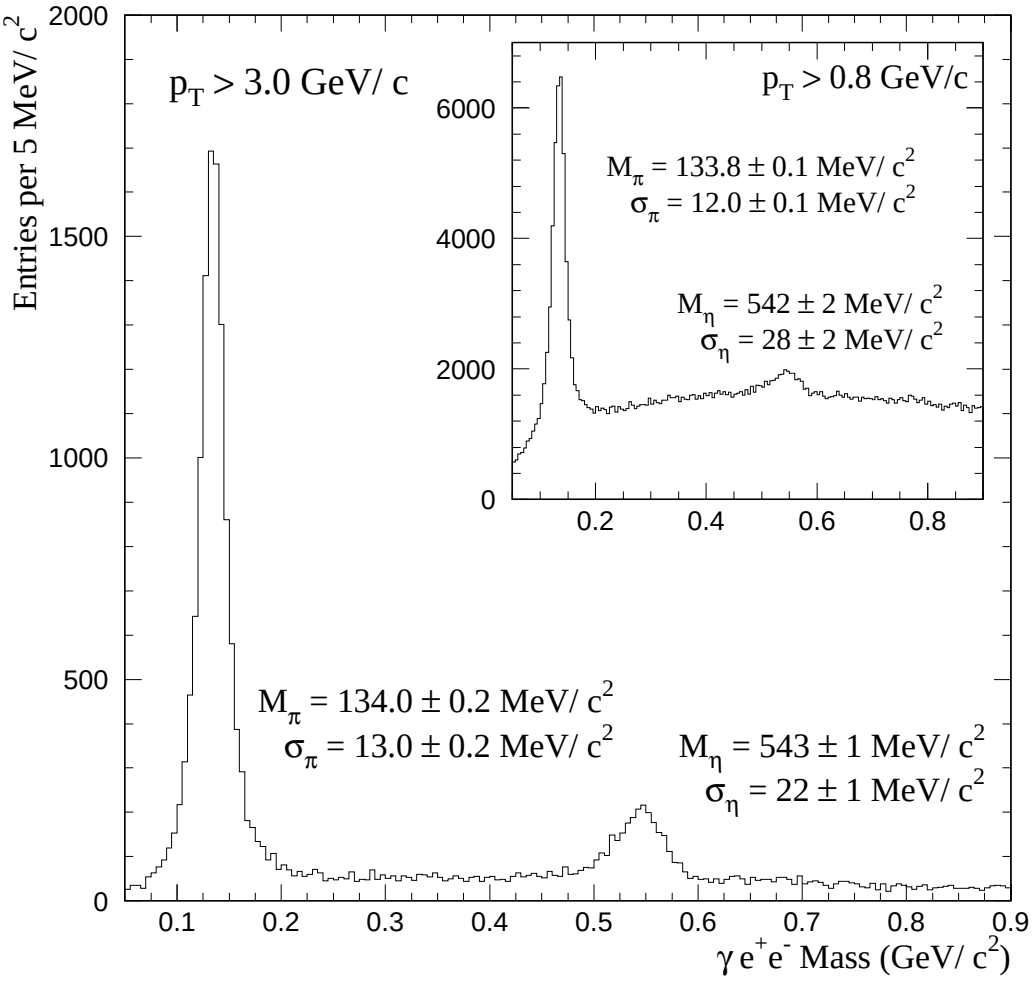

Fig. 15. The reconstructed γe^+e^- mass for low mass e^+e^- pairs from γ conversions in the target region. These γe^+e^- combinations have $P_{\rm T} > 3.0$ GeV/c. The inset shows the corresponding distribution for γe^+e^- combinations with $P_{\rm T} > 0.8$ GeV/c.

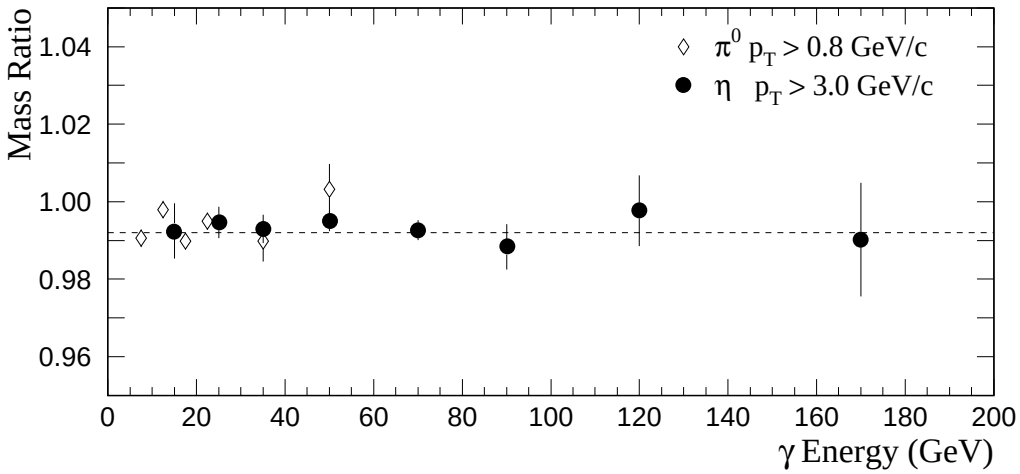

Fig. 16. Ratio of the mass of the η and away-side π^0 signals to their nominal values, for mesons detected as a γ in the EMLAC and a ZMP (due to a converted photon) reconstructed in the tracking system, as a function of the unconverted γ energy. The reconstructed masses are expected to be below nominal due to electron bremsstrahlung in the target material. The dashed line represents the mean reconstructed η mass for this sample.

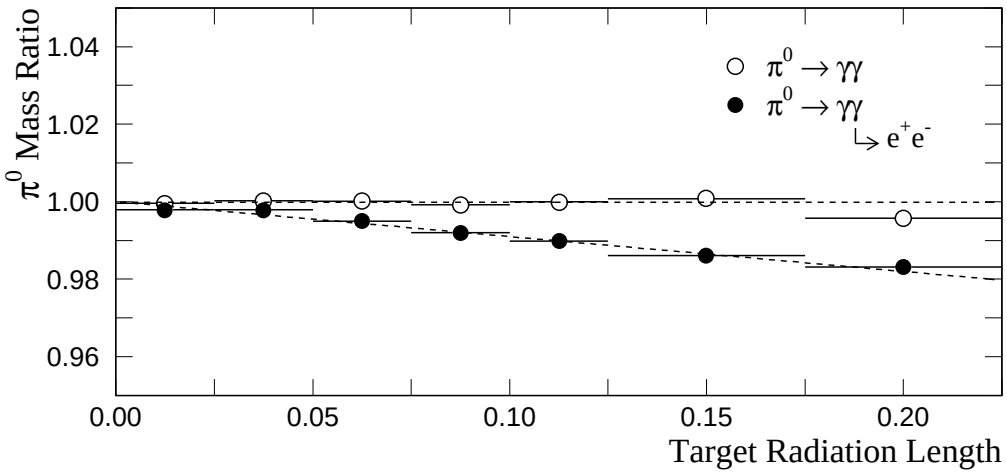

Fig. 17. The reconstructed mass of the π^0 signal relative to the PDG value as a function of the number of radiation lengths between the production point and where the daughter particles emerge from the target. Open circles represent $\pi^0 \rightarrow \gamma\gamma$ combinations where both γ's are reconstructed via the EMLAC, while the solid circles are for π^0 decays where one of the γ's converts into an e^+e^- pair that is measured in the tracking system. The lines are linear fits to the data.

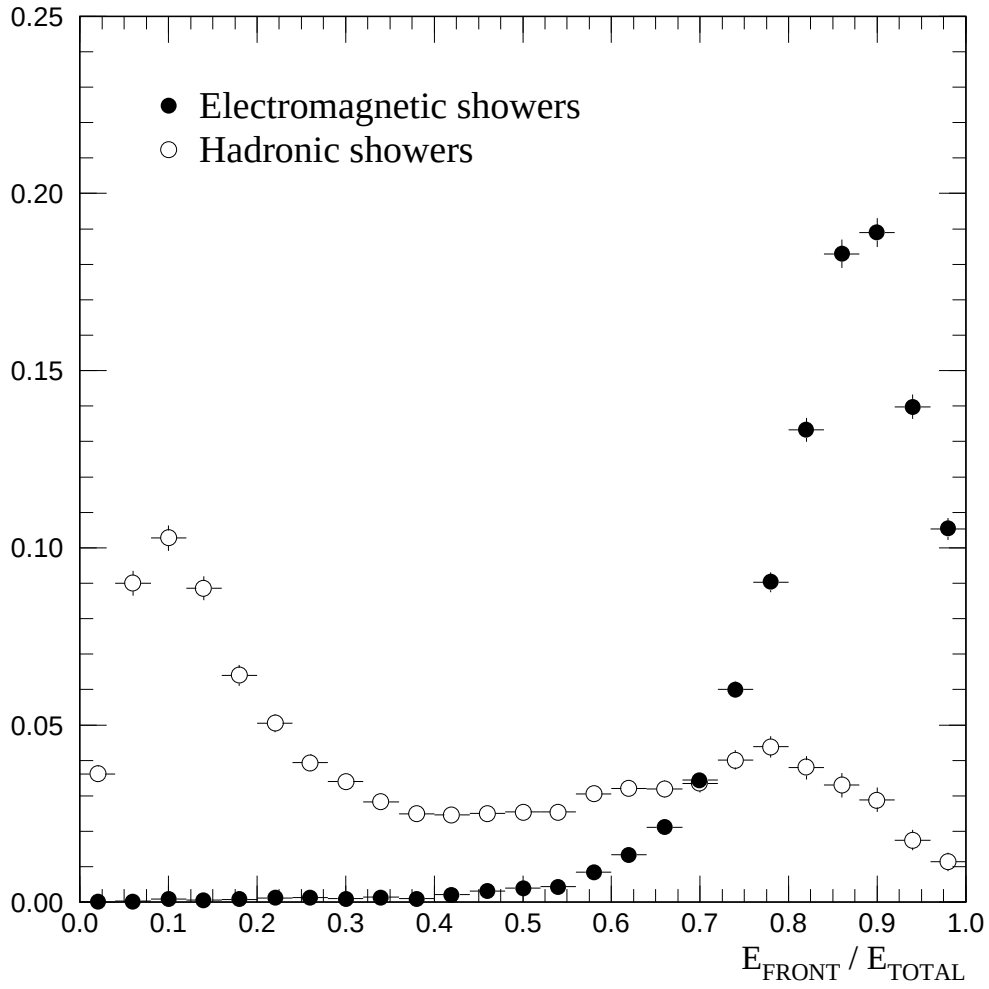

Fig. 18. $E_{\rm front}/E_{\rm total}$ distribution for ($\bullet$) electromagnetic showers from ZMP electrons and ($\circ$) hadronic showers from $\pi^{\pm}$ daughters of K^0_S decays. Each of the distributions has been normalized by the number of entries in that distribution.

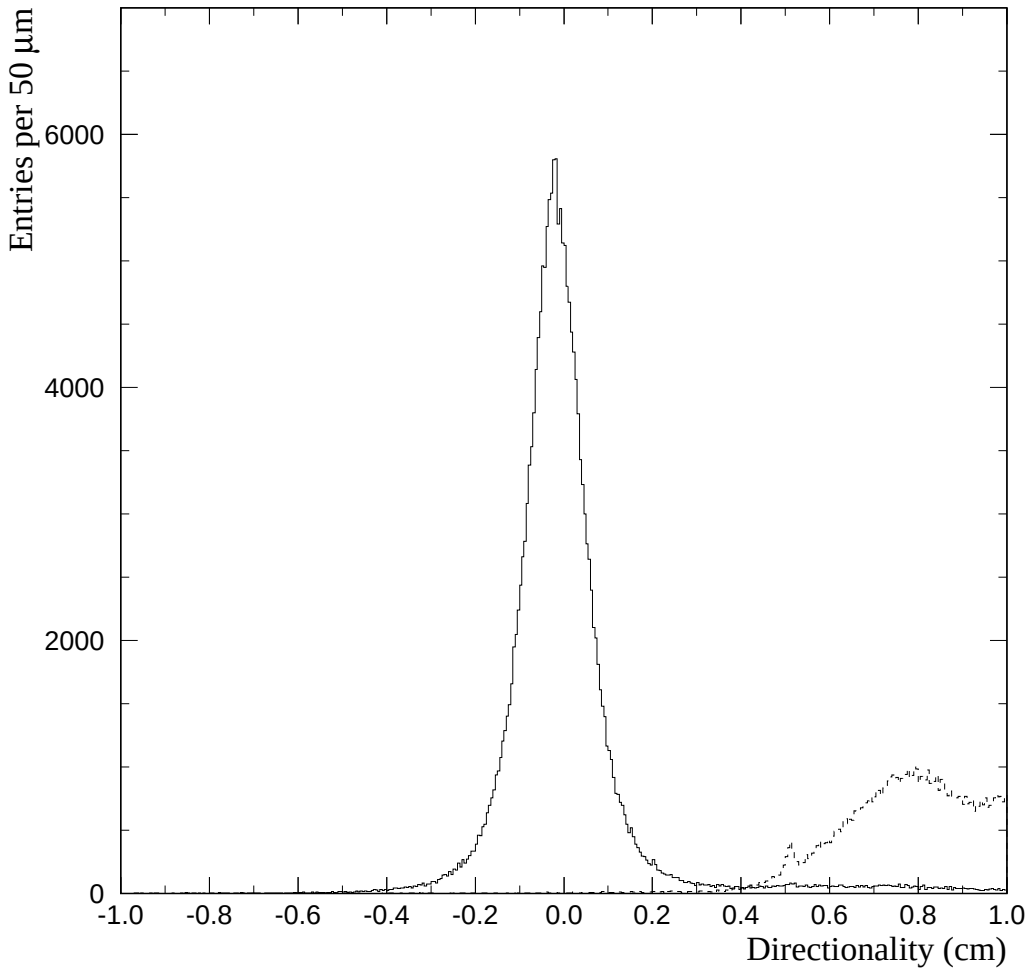

Fig. 19. The "directionality" (δ) distribution for reconstructed photons (solid histogram) and showers attributed to beam halo muon bremsstrahlung (dashed histogram). Each shower has a calculated $P_{\mathrm{T}} > 4$ GeV/c when the shower is assumed to have originated in the target.

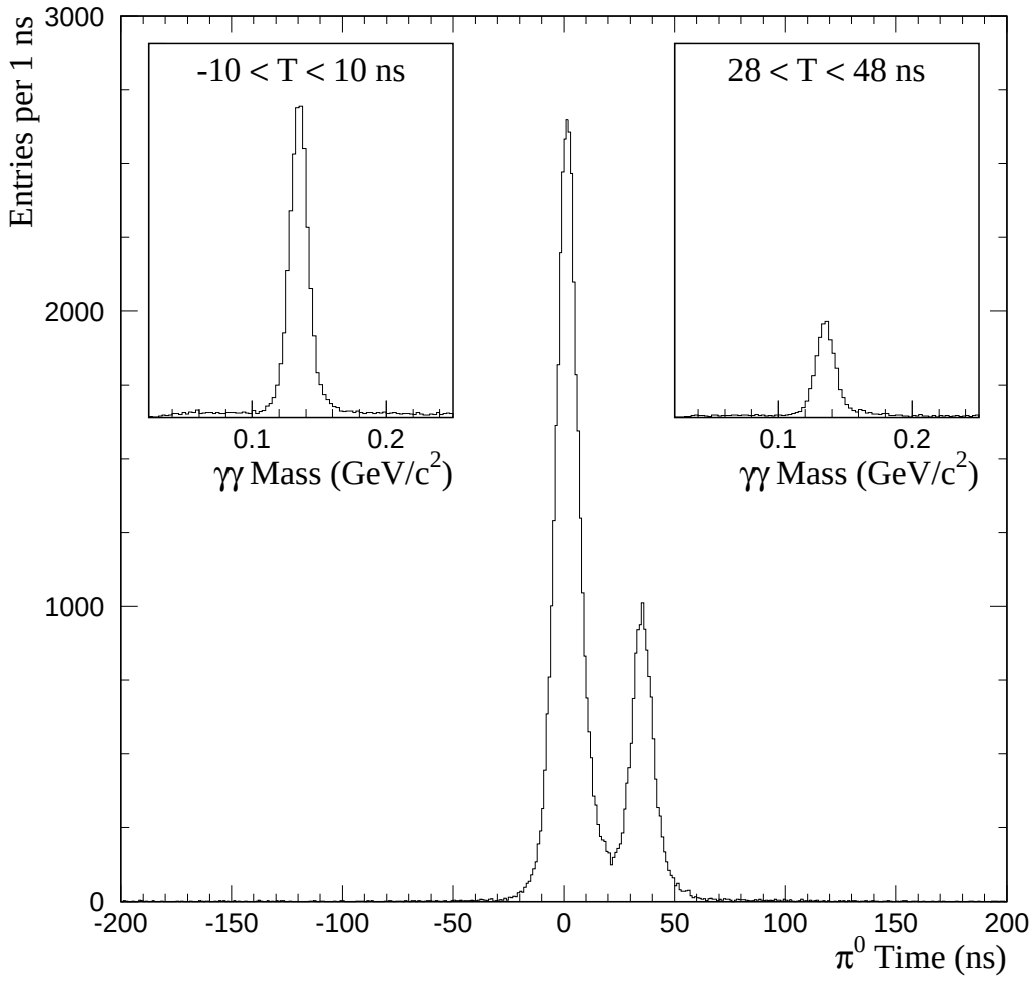

Fig. 20. The distribution of the times assigned to π^0's having $P_{\rm T} > 3$ GeV/c for events selected because there were two detected interactions—one in-time (0 ns), and one $\approx$38 ns later. Insets show the $\gamma\gamma$ mass distributions for combinations restricted to the indicated TVC time intervals.

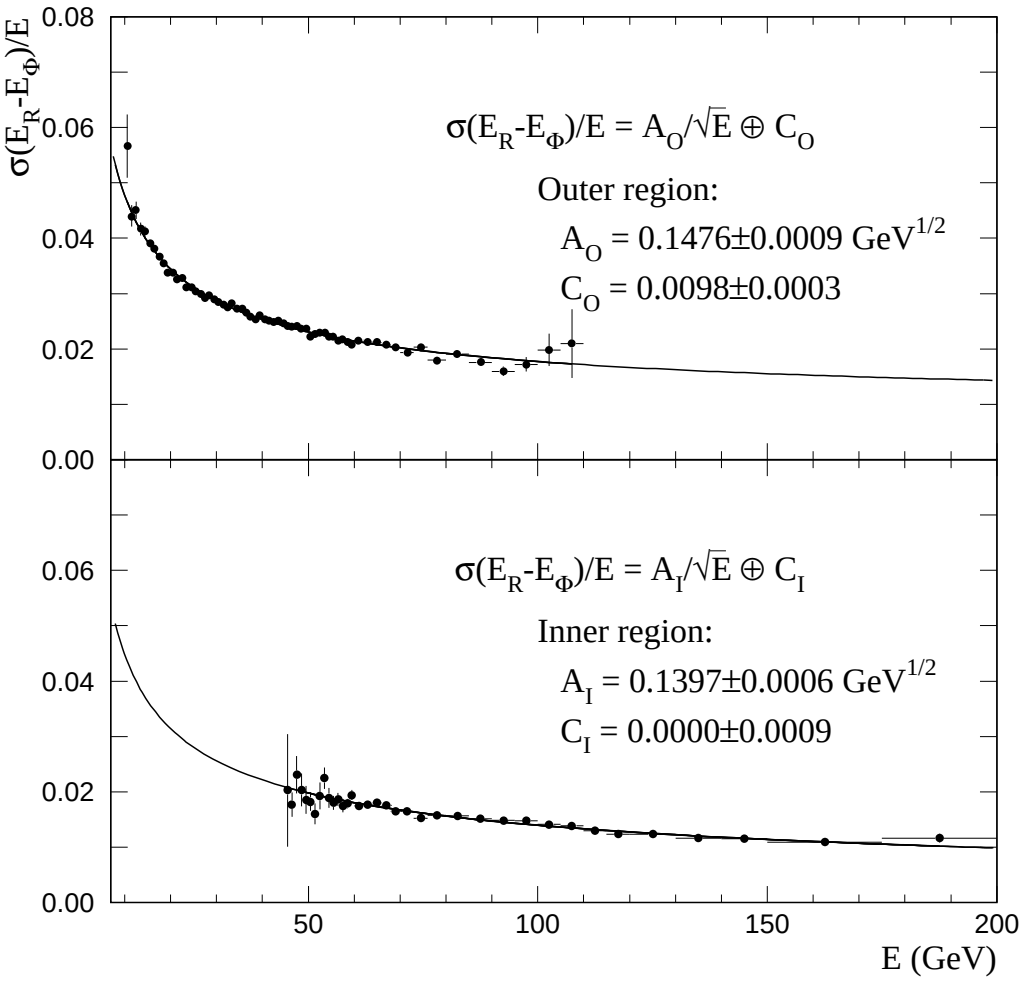

Fig. 21. Fractional widths of the $E_R - E_\Phi$ distributions plotted as functions of the total energy of the shower ($E = E_R + E_\Phi$), for showers in the outer and inner regions of the detector. The data are isolated single photons from the 1990 data sample. The curves represent the results of fits to the data with B set to zero.

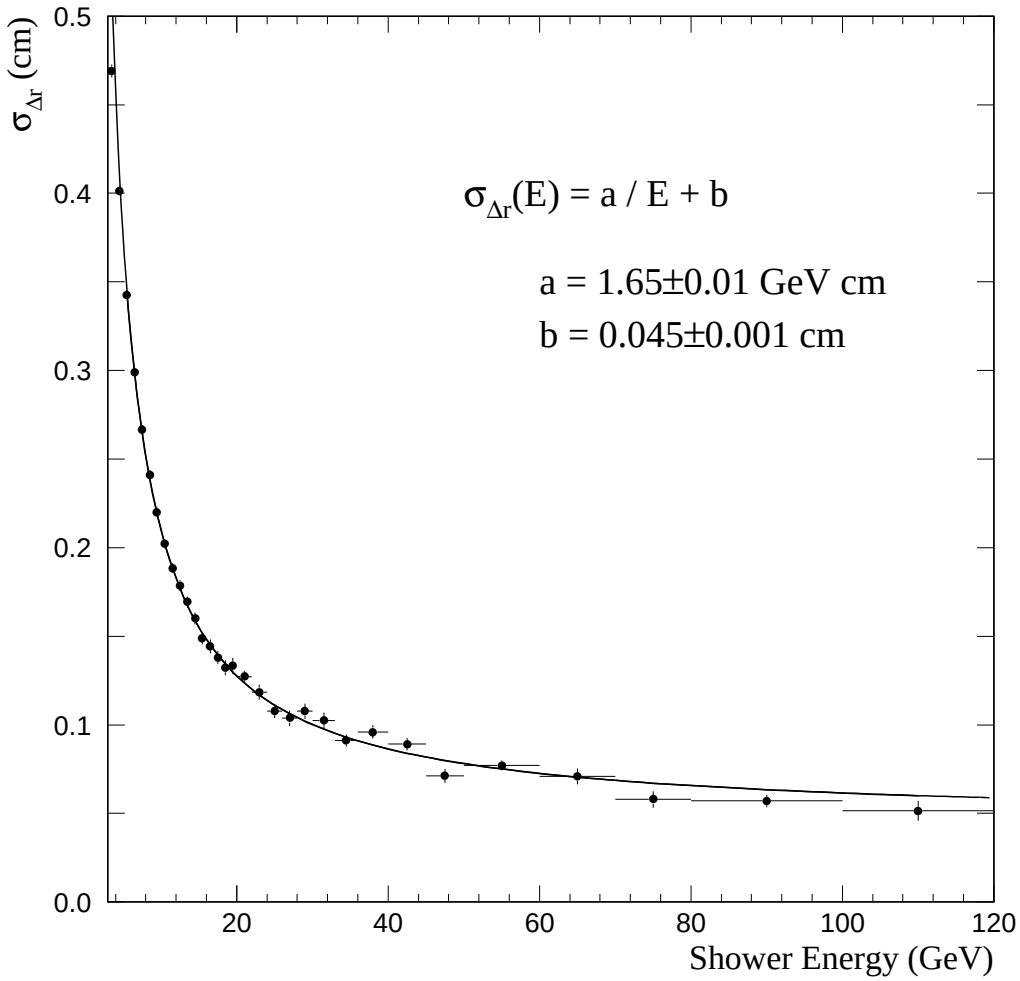

Fig. 22. EMLAC position resolution as a function of shower energy.

Table 1
The PDG mass values for the π^0, η, and ω and the reconstructed masses of these neutral mesons with $P_T > 5$ GeV/c after calibration of the EMLAC response for both the 1990 and 1991 runs of E706. The quoted masses result from fits using a gaussian and a linear background for the π^0 and η and a quadratic background under the ω.

	Nominal Mass	Reconstructed Mass	
	PDG [25]	1990 Data	1991 Data
	(MeV/c^2)	(MeV/c^2)	(MeV/c^2)
π^0	134.976±0.001	135.02±0.06	134.94±0.03
η	547.45±0.19	547.0±0.4	547.5±0.3
ω	781.94±0.12	779±5	778.5±2.5